LEAST-SQUARES METHODS FOR THE EXTRACTION OF SURFACE CURRENTS FROM CODAR CROSSED-LOOP DATA: APPLICATION AT ARSLOE

Belinda J. Lipa and Donald E. Barrick

Reprinted from IEEE Journal of Oceanic Engineering, Vol. OE-8, No. 4, October 1983

Least-Squares Methods for the Extraction of Surface Currents from CODAR Crossed-Loop Data: Application at ARSLOE

BELINDA J. LIPA AND DONALD E. BARRICK, MEMBER, IEEE

(Invited Paper)

Abstract—Least-squares methods are demonstrated that extract surface current radial velocities from first-order Coastal Ocean Dynamics Applications Radar (CODAR) sea-echo Doppler spectra for the compact crossed-loop/monopole antenna system. Based on the known physics of first-order sea scatter at HF, these techniques, implemented as software, are objective and automatic in that they: a) determine from the sea-echo phase and amplitude correction factors for the antenna elements; b) separate the first-order spectrum from the surrounding continuum for arbitrarily varying current conditions; c) using statistical hypothesis testing, select and use either a single or dual-angle model for radial current patterns, whichever best fits the data; d) calculate angles associated with given radial velocities; e) combine the data into a polar-coordinate map of radial velocity versus position; and f) calculate radial velocity uncertainties at each point on the map. In addition, as interpretive aids, two methods are evaluated and compared that provide total current vectors from single-site CODAR data, along with their uncertainties: model fitting and the application of the equation of continuity. It is shown how these methods can be applied to the older, CODAR 4-element antenna system, however, the following advantages of the crossed-loop/monopole system are discussed: it is physically more compact; analysis procedures are more efficient; resulting current velocities are more accurate, because there are no side-lobe problems; and finally, it also gives the ocean wave-height directional spectrum.

These methods are tested and optimized against data taken during the Atlantic Remote Sensing Land Ocean Experiment (ARSLOE) storm (October 23–27, 1980), when surface currents varied in speed between 0–50 cm/s and over nearly 300° in angle. Current velocities were measured to a range of 36 km from the radar. Standard deviations in angle are typically 1°–3°; these translate to 2–3 cm/s rms radial velocity uncertainties over most of the coverage area, with decreased accuracy in angular sectors nearest the coast. Total current velocity vectors in strips parallel to shore obtained from model fitting have typical speed and angle uncertainties of 4 cm/s and 12°, respectively. Of the several formulations for the equation of continuity evaluated here, the best gave uncertainties of 5 cm/s, 12° at the closest range cells; these values increase rapidly with range to exceed 20 cm/s, 30° for distances greater than 20 km.

The surface currents were observed to follow the wind throughout most of the storm at ARSLOE, but the current was almost always more closely parallel to the shore than the wind. An interesting exception occurred when the onshore storm wind that had prevailed for two days ceased; there was a rush of surface current directly offshore as the storm-surge sea level dropped. The surface current speed measured by CODAR in the upper meter of the ocean was, on the average, 2.1 percent of the windspeed.

Manuscript received March 7, 1983; revised July 28, 1983. This work was supported in part by the NOAA Coastal Waves Program, and in part by Gulf Oil Exploration and Production Company.

B. J. Lipa is with Ocean Surface Research, Woodside, CA 94062.
D. E. Barrick is with Ocean Surface Research, Boulder, CO 80303.

I. INTRODUCTION

THE MEASUREMENT of currents near the ocean surface is difficult using conventional systems, and the formation of fine-resolution current maps at a given point in time has been virtually impossible. These currents in the upper meter are highly variable temporally as well as spatially, being driven (as are all currents) by geostrophic forces, tides, and runoff from rivers, but especially influenced by the local surface wind and wave fields. Tracking of dye and drifting buoys has been employed historically, but gathering and interpreting such data (either with shore-based or aircraft/spacecraft sensors) is expensive for the sparse spatial sampling provided. Near shore where considerable maritime activity occurs, routine continuous monitoring of surface currents in both space and time is becoming increasingly desirable.

Nearly three decades ago, Crombie [1] discovered experimentally that HF radar signals backscattered from the rough, moving sea surface select as their dominant targets ocean wavetrains (or spectral components) of precisely half the radar wavelength λ. Spectrally analyzed, these first-order sea-echo signals appear as dominant peaks surrounded by a continuum due to higher order scatter and noise. In the absence of ocean surface currents, the first-order peaks occur at two discrete frequency positions symmetrically arrayed about the radar carrier frequency. Their displacements, or Doppler shifts, are directly proportional to the phase velocity of the Bragg-scattering ocean wavetrains, of $\lambda/2$ wavelength, through the gravity-wave dispersion equation. Barrick [2] related their amplitudes to the wave height directional spatial spectrum evaluated at the Bragg wavenumber $2k_0$ $(=4\pi/\lambda)$. Crombie [3] first showed that a smaller Doppler shift detectable by HF radars was a measure of currents transporting the Bragg-scattering ocean waves; he demonstrated this qualitatively with a small, 2-element, direction-finding receiving antenna by looking at the strong flow of the Gulf Stream east of Florida. In this sense, the scattering ocean waves are tracers of the underlying currents moving radially toward the radar, much as chaff reflectors are used to detect wind velocities with microwave radars. Narrow-beam radar investigations at San Clemente Island by Stewart and Joy [4] and Barrick *et al.* [5] proved the qualitative accuracy of this technique, and demonstrated that currents in layers of varying depth could be measured by changing the radar operating frequency, and hence the wavelength of the Bragg-scattering ocean waves. Narrow-beam radars at HF have antennas hundreds of meters long; their

0364-9059/83/1000-0226$01.00

practicality for coastal and offshore applications is therefore limited. Skywave narrow-beam radars at HF use ionospheric reflections to observe the ocean to distances of thousands of kilometers. Ocean wave parameters can be extracted from skywave echo, but measurements of current velocities are complicated by unknown ionospheric movements; usually current measurement of coarse spatial resolution is possible only in the vicinity of fixed targets such as land, islands [6]. Narrow-beam dual-frequency microwave radars have successfully measured surface current velocities with a high degree of spatial resolution [7], [8], but the observations are limited to line of sight.

In order to adapt HF radar to fill the need for monitoring coastal currents, NOAA's Wave Propagation Laboratory began a program in 1975 to develop a compact, transportable system that could map surface currents in near-real time. Called CODAR (Coastal Ocean Dynamics Applications Radar), this system operated at ~25 MHz, thereby backscattering from ~6-m ocean waves [9]. Using small (and hence nearly omnidirectional) separate transmit and receive antennas, this system determined the bearing to a scattering element with a given Doppler frequency by using a 4-element direction-finding antenna concept [10]. With a range of ~60 km from shore, this system has been used successfully in some 14 experiments.

In later efforts to extend CODAR to measure coastal ocean wavefields [11], an even more compact antenna system was devised, consisting of three elements: two crossed loops and a monopole, which will be referred to as the CODAR loop system. It measures ~2-m high and ~0.6-m laterally. (See Fig. 1) This antenna forms and scans a beam electronically, rather than relying on the earlier direction-finding concepts. It was initially envisioned only for monitoring the waveheight directional spectrum from the second-order echo. However, variation of radial currents across the broad beam was found to degrade the wave spectral resolution obtainable in some situations, and hence we began developing methods to measure the surface currents from the first-order echo so that they could be removed from the second-order echo. In the process, we found that the loop system can in fact measure surface currents with several advantages over the previous NOAA 4-element system. This paper develops, presents, and demonstrates the analysis methods that accomplish this, starting with the voltage time series from the three antennas and ending with current velocity maps.

The analysis is automatic throughout, including derivation of hardware calibration factors from the sea echo and the isolation of the first-order spectrum from the surrounding continuum. Signal analysis is based on the least-squares method and provides an objective treatment of all available data using the known signal statistics. These methods require detailed knowledge of the statistical distribution of the signal, its covariance matrix and correlations as a function of range and frequency. Theoretical expressions are given for these quantities; we verify the theory by analyzing unaveraged experimental data. The random nature of the signals originates because the sea echo itself is a Gaussian random variable [17] and contains an additive Gaussian noise component. The signal uncertainties are propagated through the analysis, and must be traced throughout, firstly in order that the data may be properly combined at each stage and secondly so that uncertainties in the final results will be available. This is easily accomplished with standard least-squares procedures. The end result is a current velocity map with uncertainties provided at every point.

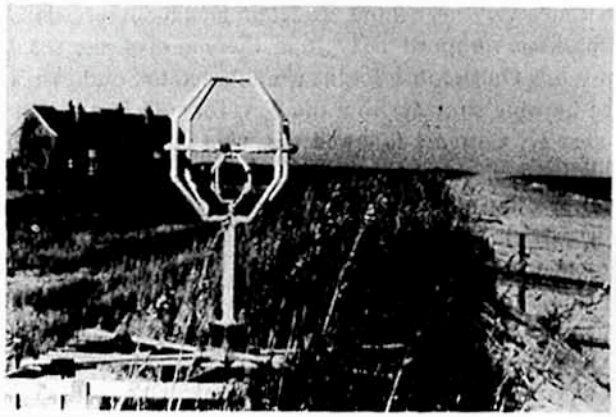

Fig. 1. Photograph of the CODAR crossed-loop/monopole antenna at ARSLOE. Vertical height is ≈2 m. Efficient operation at 25-26 MHz is achieved by inductive energy coupling from the large copper outer loops via the smaller inner loops.

The analysis presented here is the first complete statistical treatment of data from a CODAR system. Numerous comparisons have been made between CODAR measurements made by the NOAA 4-element system and other instrumentation [9], [13]-[16]; these intercomparisons show agreement in velocity ranging between 5 and 25 cm/s. Instrument intercomparisons have only a limited use in the interpretation of CODAR velocity uncertainties, however, since different environmental conditions (winds/waves) varying with time and position on the ocean can significantly change the accuracy of CODAR results. In addition, it has been mentioned [13] that use of different processing software on the same data set can lead to nontrivial differences in the extracted radial current velocities, clearly indicating the need for error estimation. What is really required is an estimate in the uncertainty of each current vector every time a map is produced. Analysis methods for the NOAA 4-element system have been based on closed-form calculations of signal direction [9], [10], [16] and do not readily provide estimates of uncertainty from the sea-echo data. This is one of the important advantages of least-squares techniques; we show in this paper how our methods could be applied directly to the NOAA 4-element system to give least-squares estimates of current velocities and their uncertainties; however, we also show that analysis of data from the loop system is simpler and more accurate.

ARSLOE provided particularly interesting conditions with which to develop and demonstrate our methods for extracting currents. Only one CODAR site was deployed, since we originally intended to measure only the ocean wave spectrum at ARSLOE; normal CODAR measurement of surface currents involves the combination of vectors from two sites to give the total current velocity. Over a period from October 22 through October 27, 1980, a storm occurred off the Eastern coast. Starting from very calm, quiescent wave and current conditions, the wind began blowing steadily toward shore from the Northeast at 10-15 m/s for ~60 h, developing strong wave and storm-driven currents; the latter opposed the normal flow

in that area very near shore, as determined by observations of dye packages dropped daily from the end of a pier 0.5 km from shore. On October 25, the wind turned to Southeast, and ended blowing strongly from the West for ~36 h, quieting by October 27. Currents followed the wind in direction, ending finally in their normal pattern near shore: South to North. Therefore, the radial current velocity spread and the directional pattern varied considerably over this period, allowing us to exercise and optimize our algorithms under a wide range of conditions. Finally, since we had data from only one site, we developed and evaluated two methods for deducing total current vectors and their uncertainties from single-site CODAR data at ARSLOE: model-fitting and application of the equation of continuity. The total current vectors derived provide a consistent picture of coastal surface-current patterns that develop under a rather complex storm.

Fig. 2 is an example of the sea-echo Doppler power spectrum measured at ARSLOE during the storm on the monopole antenna. Having a spectral resolution of 0.00745 Hz, this plot is an average of 16 individual power spectra at sequential times 134 s apart. Recorded when the wind was blowing onshore from 25° North of the perpendicular to the coast at ~12 m/s for ~30 h, this spectrum illustrates the typical features of CODAR sea echo: a) dominant first-order peaks, somewhat broadened by currents and stronger on the positive Doppler side because of onshore winds and waves, and b) a pronounced second-order region resulting from the storm waves present (with ~3-m significant waveheight). The ocean current velocities in a range cell are obtained from the first-order spectrum as follows: the Doppler frequency of each spectral point defines a value of radial current velocity; the sea echo received by the broad-beam antennas at a given frequency comes from one or more directions, which are derived from the data using the known antenna patterns. This gives the angle as a function of radial velocity; the inversion of this function gives the velocity versus angle, i.e., the current map.

In the next section we present a description of the CODAR loop antenna system, as it was developed for and operated at ARSLOE. Section III gives a theoretical description of the physics and resulting analytical methods used for extracting surface currents from the loop system. In Section IV we describe the application of these methods to the ARSLOE data set and present the resulting current patterns observed by CODAR during the October storm. In order that this manuscript can serve as a self-contained reference, we support general descriptions of the methods given in the text with detailed appendices. Appendix A presents elements of those least-squares and error-propagation methods that we have employed for estimating data products and uncertainties. Appendix B gives statistical properties of cross spectra that we use to derive the data covariance matrix for uncertainty calculations. Appendix C verifies the statistical theory on which the analysis methods are based by treating unaveraged data measured at ARSLOE. Appendix D describes an automatic technique for separating the first-order spectrum from the surrounding continuum; this method is based on knowledge of the nature of the spectrum (both sea-echo and noise) and can be applied for varying current regimes. Appendix E shows how these methods can be applied to give the same data products and uncertainties from the CODAR 4-element system.

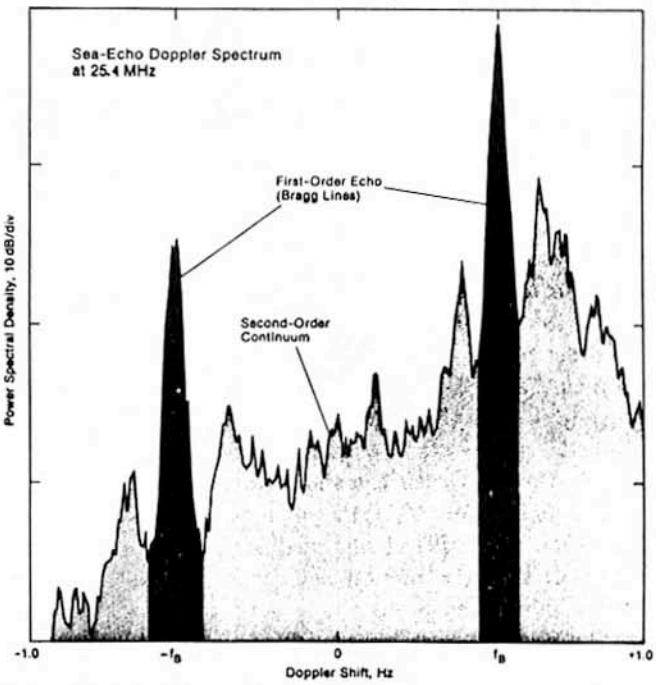

Fig. 2. Example of a sea-echo Doppler spectrum measured at ARSLOE with the monopole antenna on October 24, 19:80 GMT, when winds and waves were onshore from 0:45 T. Sixteen independent power spectral samples were averaged to produce the spectrum; the frequency resolution is 0.007451 Hz and the Bragg frequency is 0.514 Hz.

II. THE CODAR LOOP SYSTEM AT ARSLOE

The actual hardware for the loop antenna system deployed at ARSLOE was a considerable improvement over that used in an earlier CODAR experiment at Pescadero, CA, during January, 1978 [11], [22]. As described in [11], a loop that is sufficiently small electrically to have a cosine radiation pattern (i.e., appear as a magnetic dipole) also has a very low radiation resistance. With the circumference less than 0.3 times the radar wavelength, the radiation resistance is of the order of 1 Ω or less, although the inductive part of the impedance is much higher. In the process of eliminating the inductive reactance by resonating with an equal capacitive reactance, and transforming the remaining resistive component up to standard transmission-line values, small ohmic resistances in the wires become larger along with the radiation resistance. Therefore, small loop systems are lossy; the system operated at Pescadero was some 20 dB less efficient than a monopole resonant at the same frequency (i.e., 25.4 MHz).

One way of reducing ohmic losses and therefore increasing efficiency is to increase the copper conductor diameter, to the point where it is in effect a pipe; that used at ARSLOE was hollow, with an outer diameter of approximately 4 cm. The method of feeding a single loop efficiently was developed and patented by Antenna Research Associates [23]; this method employs a much smaller, inner loop near the base of—and coplanar with—the larger loop. Therefore, there is no direct line excitation of the main, radiating loop; capacitive tuning occurs

at the top of the outer loop. This design allows the loop to radiate 2-3 dB *more* efficiently than a quarter-wave monopole.

The primary and truly novel adaptation of this proven, single-loop technique to our CODAR application was designed and patented by Carr [24]. This puts two such rigid pipe loops (each with its smaller, coplanar exciting loop) in orthogonal planes, as shown in Fig. 2. Again, each loop is tuned separately by capacitors at the top of the outer loops. The copper pipes in the outer loop structures are welded together. No insulation is necessary to isolate the outer radiating loops because they are geometrically orthogonal to each other; electrical tests showed the isolation between them to be better than 50 dB.

Unlike the Pescadero antenna system in which an electrically separate short monopole was located beneath the two loops (colinear with the intersection of their planes), here the copper stem below is simply welded to the crossed-loop frame. The entire structure, all electrically continuous, therefore serves as the "monopole", or E-field radiator. The symmetrical, electrically small crossed-loop frame on top of the vertical frame acts much like "top-hat" radials sometimes used on a monopole, serving to reduce its resonant length and increase its bandwidth somewhat. Therefore, there is no electrical insulation anywhere between the three effective elements (two loops and the monopole) that comprise the upper radiating structure. A 4-element quarter-wavelength radial counterpoise (located in the same planes as the crossed loops) served as both the ground plane for the monopole and as a mechanical stand for the vertical structure. Standing less than 2 m in height, the device weighs about 20 kg.

The pattern of the "monopole" was observed to be indeed isotropic. The loop power patterns were measured on a turntable in Boulder, and are shown in Fig. 3. Departures from the desired cosine-squared pattern are always less than 10 percent in power, with a standard deviation between the measured and desired over the entire patterns of ~2.7 percent. At ARSLOE, the structure was operated from a dune ridge parallel to the water, about 5 m in height and back about 30 m from the water. At the site the power pattern was again verified by tests with a transponder on a boat that took up different azimuthal positions at constant range.

This crossed-loop/monopole structure is used only for reception. Transmission is accomplished with an omnidirectional monopole located about 30 m away. The loop planes were positioned approximately 45° with respect to the straight coastline. Power probes were located 80 m away, on the shoreward side, one each in the loop planes and one bisecting the planes (along the perpendicular to the coast). These were used periodically over the two-month experiment to verify that the antennas were functioning properly.

During radar operations, 8-μs pulses were transmitted every 2^9 μs. One each of the three antenna elements were sequentially sampled after transmission of each pulse, along with a fourth dummy-load port, to receive the signal over the time span between consecutive transmitted pulses. Each receiving element was thus revisited every 2^{11} μs. For sea echo with a typical Doppler spectrum between ±1 Hz from the carrier, reception on "sequential" pulses this close together is therefore considered "simultaneous". Because the CODAR system at that time retained only 32 range samples (starting from shore), we could analyze data out to 37.8 km with our 8-μs pulsewidth.

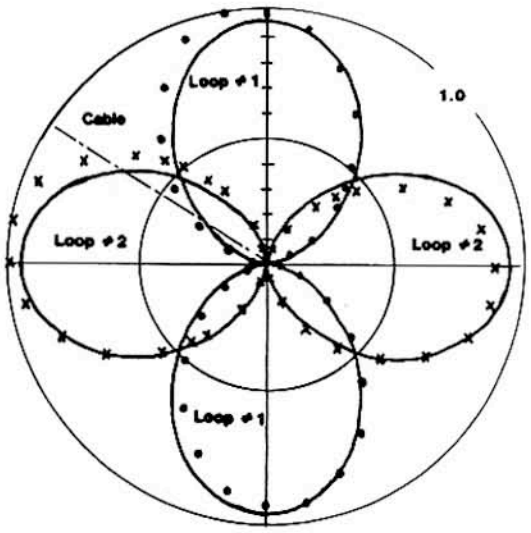

Fig. 3. Power patterns for the crossed-loops measured on a turntable (dots and crosses) compared to the theoretical cosine-squared prediction; scale is linear in normalized power, with circles at 1.0 and 0.5. Position of feed cable beneath the antenna (shown by the dashed line) may have caused the slight distortions from ideal.

The loop radiation patterns must have equal amplitudes with each other at their maxima and also with the monopole; their phase differences must all be zero (for the positive loop lobes). In reality, because of the symmetrical design, the crossed loops always maintained the desired amplitude/phase relationships to each other during normal operations. The slight departures from the cosine-squared power patterns, and the continuous but rapid phase transition that approximates the theoretical 180° discontinuity at the null between the positive and negative lobes, were studied in simulations. These departures from ideal were shown to produce biases in the data (in angle of arrival) that are less than the standard deviation due to the sea-echo's statistical fluctuations, and hence can be ignored. The amplitude and phase mismatches between the loops and the monopole were not eliminated in hardware; it is much easier to remove these in the software (as described subsequently) than to attempt to keep the hardware matched. Both the sea-echo data, the probe tests, and the ship calibration tests showed that indeed these loops are more efficient antenna elements than the monopole, by 1-2 dB.

III. ANALYSIS TECHNIQUES FOR THE CODAR LOOP SYSTEM

This section gives a complete description of analysis techniques used to produce current vector maps from the voltage time series measured by the three antennas. In Section III-A we describe initial data processing: the analysis starts with the Fourier-transformation of the voltage time series and the formation of conjugate voltage products (or cross spectra), followed by the combination of signals to effect the rotation of a broad beam over the ocean surface. The angular Fourier coefficients of the broad-beam return are then calculated; these may be regarded as convenient intermediate data prod-

ucts. We show how to obtain expressions for the covariance matrix of these coefficients. Section III-B describes how radial current velocities are obtained from the Fourier angular coefficients; statistical uncertainties in these quantities follow from the known covariance matrix of the data. Finally, in Section III-C, we discuss methods for deriving total current velocities from the radial components.

A. Formation of Fourier Angular Coefficients

1) Conjugate Voltage Products: Voltage time series from the three antennas are Fourier transformed to give complex frequency spectra $\mathring{V}_i(\omega)$, where ω is the frequency and $i = 1, 2, 3$ denotes the two loops and the monopole, respectively. Each spectral value is a complex Gaussian random variable. Conjugate products of the voltages are then formed; they are cross-spectral estimates of infinite ensemble averages $\langle \mathring{V}_i(\omega)\mathring{V}_j^*(\omega)\rangle$. Before further analysis, the amplitude of the antenna patterns must be adjusted to be equal at their beam maxima and relative phase corrections applied to equalize the phase paths. It is only the relative gain between the loops and the monopole which must be equalized; the absolute value of the monopole beam maxima is irrelevant to this analysis.

A single electrically small loop has a voltage pattern which varies as cos ϕ where the angle ϕ is taken relative to the beam maximum; the crossed loop at right angles has a pattern sin ϕ with respect to the same axis. The complex voltage spectra at any frequency can be expressed in terms of the sea-echo pattern as follows:

$$\mathring{V}_1(\omega) = \frac{1}{2\gamma}\int_{-\gamma}^{\gamma} \cos\phi \mathring{g}(\omega,\phi)\,d\phi \tag{1}$$

$$\mathring{V}_2(\omega) = \frac{1}{2\gamma}\int_{-\gamma}^{\gamma} \sin\phi \mathring{g}(\omega,\phi)\,d\phi \tag{2}$$

$$\mathring{V}_3(\omega) = \frac{1}{2\gamma}\int_{-\gamma}^{\gamma} \mathring{g}(\omega,\phi)\,d\phi \tag{3}$$

where $\mathring{g}(\omega, \phi)$ is the complex, narrow-beam sea-echo, vertically polarized E-field return at a given angle and γ is the angle subtended by the coastline at the radar (Fig. 4). In the presence of phase and amplitude mismatches of the loops with respect to the monopole, the right-hand sides of (1) and (2) must be multiplied by the complex correction factors $a_1 e^{i\theta_1}$ and $a_2 e^{i\theta_2}$. We will now describe how these factors may be calculated from the data.

The measured squared voltage can be written as follows:

$$\langle|\mathring{V}_1(\omega)|^2\rangle = \frac{{a_1}^2}{(2\gamma)^2}\int_{-\gamma}^{\gamma} d\phi_1 \int_{-\gamma}^{\gamma} d\phi_2 \cdot \langle \mathring{g}(\omega,\phi_1)\mathring{g}^*(\omega,\phi_2)\rangle \cos\phi_1 \cos\phi_2 \tag{4}$$

where the angular brackets denote infinite ensemble averages. Barrick and Snider [17] have shown that the sea echo is uncorrelated for angular separations as small as 0.5°; therefore

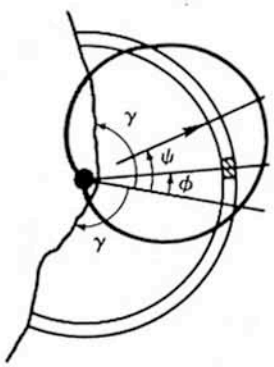

Fig. 4. Sketch of the beam pattern. A circular range ring is shown. The scan angle ψ, the coastline angle γ, and a general angle ϕ are defined with respect to the bisector of the partial ring of sea.

(4) reduces to

$$\langle|\mathring{V}_1(\omega)|^2\rangle = \frac{{a_1}^2}{2\gamma}\int_{-\gamma}^{\gamma} \cos^2\phi\,\sigma(\omega,\phi)\,d\phi \tag{5}$$

where we have written

$$\frac{1}{2\gamma}\langle \mathring{g}(\omega,\phi_1)\mathring{g}^*(\omega,\phi_2)\rangle \equiv \sigma(\omega,\phi_1)\delta(\phi_2-\phi_1) \tag{6}$$

where $\sigma(\omega, \phi)$ is the narrow-beam radar cross section, with similar relationships for the other antennas

$$\langle|\mathring{V}_2(\omega)|^2\rangle = \frac{{a_2}^2}{2\gamma}\int_{-\gamma}^{\gamma} \sin^2\phi\,\sigma(\omega,\phi)\,d\phi \tag{7}$$

$$\langle|\mathring{V}_3(\omega)|^2\rangle = \frac{1}{2\gamma}\int_{-\gamma}^{\gamma} \sigma(\omega,\phi)\,d\phi. \tag{8}$$

Combining (5), (7), and (8) gives

$$\langle|\mathring{V}_3(\omega)|^2\rangle = \frac{\langle|\mathring{V}_1(\omega)|^2\rangle}{{a_1}^2} + \frac{\langle|\mathring{V}_2(\omega)|^2\rangle}{{a_2}^2}. \tag{9}$$

The amplitude mismatch factors are obtained by fitting (9) to the data using the least-squares techniques described in Appendix A. In our analysis we used the strong signal surrounding the Bragg frequencies. Use of (9) is not limited to first-order sea echo, however; it can also be used with second-order echo, the only requirement being that the signal decorrelate with azimuth angle according to (6).

To obtain the phase angle corrections θ_1, θ_2 of the loops relative to the monopole from the data, the mean phase angles of $\langle\mathring{V}_1(\omega)\mathring{V}_3^*(\omega)\rangle$ and $\langle\mathring{V}_2(\omega)\mathring{V}_3^*(\omega)\rangle$ are calculated as an average over frequency. The phase angle of $\langle\mathring{V}_1(\omega)\mathring{V}_2^*(\omega)\rangle$ can be calculated as a check and should equal $(\theta_1 - \theta_2)$ to within a few degrees.

The complex-conjugate voltage products are then corrected for phase and amplitude mismatches: for example, the corrected

version of $\langle V_1(\omega)V_2^*(\omega)\rangle$ is

$$\langle \mathring{V}_1(\omega)\mathring{V}_2^*(\omega)\rangle_{\text{corrected}} = \frac{\langle \mathring{V}_1(\omega)\mathring{V}_2^*(\omega)\rangle}{a_1 a_2 e^{i(\theta_1-\theta_2)}}. \tag{10}$$

2) Calculation of Fourier Angular Coefficients: To scan a broad beam electronically to angle ψ (Fig. 4), we multiply $\mathring{V}_1(\omega)$ by $\cos\psi$, $\mathring{V}_2(\omega)$ by $\sin\psi$, and add to $\mathring{V}_3(\omega)$ to give the following expression for the broad-beam output at frequency ω:

$$\tilde{\sigma}(\omega,\psi) = K\langle |\, \mathring{V}_1(\omega)\cos\psi + \mathring{V}_2(\omega)\sin\psi + \mathring{V}_3(\omega)\,|^2\rangle \tag{11}$$

where K is an arbitrary constant containing such factors as system gains and path losses. The value of K is irrelevant in our analysis; therefore for simplicity it will be set it to unity. It follows from (1) (and [11]) that $\tilde{\sigma}(\omega,\psi)$ may be expressed as a Fourier series over angle with exactly five nonzero coefficients

$$\tilde{\sigma}(\omega,\psi) = \frac{1}{2\pi}\sum_{n=-2}^{2} b_n(\omega)\,tf_n(\psi) \tag{12}$$

where $tf_n(\psi)$ are trigonometric functions defined by

$$tf_n(\psi) = \begin{cases} \cos n\psi, & \text{for } n \geqslant 0 \\ \sin |n|\psi, & \text{for } n < 0. \end{cases} \tag{13}$$

Using (11) and (12) we write the following expression for the Fourier coefficients:

$$\begin{aligned} b_n(\omega) &= \frac{2}{\epsilon_n}\int_{-\pi}^{\pi} \tilde{\sigma}(\omega,\psi)tf_n(\psi)\,d\psi \\ &= \frac{2}{\epsilon_n}\int_{-\pi}^{\pi} \langle |\, \mathring{V}_1(\omega)\cos\psi + \mathring{V}_2(\omega)\sin\psi \\ &\quad + \mathring{V}_3(\omega)\,|^2\rangle tf_n(\psi)\,d\psi \end{aligned} \tag{14}$$

where

$$\epsilon_n = \begin{cases} 2, & \text{for } n = 0 \\ 1, & \text{for } n \neq 0. \end{cases}$$

Expanding the angular brackets and performing the integration in (14) relates the Fourier coefficients to the cospectra of the voltages. The cospectrum P_{ij} between two voltage spectra $V_i(\omega)$ and $V_j(\omega)$ is defined by

$$P_{ij} \equiv \langle \mathrm{Re}\,[\,\mathring{V}_i(\omega)\mathring{V}_j^*(\omega)]\rangle. \tag{15}$$

The relationship is given by

$$\begin{aligned} b_{-2}(\omega) &= 2\pi\,\langle \mathrm{Re}\,[\,\mathring{V}_1(\omega)\mathring{V}_2^*(\omega)]\rangle \equiv 2\pi P_{12} \\ b_{-1}(\omega) &= 4\pi\,\langle \mathrm{Re}\,[\,\mathring{V}_2(\omega)\mathring{V}_3^*(\omega)]\rangle \equiv 4\pi P_{23} \\ b_0(\omega) &= 3\pi\langle |\, \mathring{V}_3(\omega)\,|^2\rangle \equiv 3\pi P_{33} \\ b_1(\omega) &= 4\pi\,\langle \mathrm{Re}\,[\,\mathring{V}_1(\omega)\mathring{V}_3^*(\omega)]\rangle \equiv 4\pi P_{13} \\ b_2(\omega) &= \pi\langle |\, \mathring{V}_1(\omega)\,|^2 - |\, \mathring{V}_2(\omega)\,|^2\rangle \equiv \pi(P_{11}-P_{22}). \end{aligned} \tag{16}$$

Although we have maintained the concept of a broad beam being scanned to an angle for illustrative purposes, the scan angle and integrations over it as in (14) do not actually enter into our data analysis. The Fourier angular coefficients of the sea echo $b_n(\omega)$ are obtained as cospectra (complex-conjugate products) of the Fourier-transformed antenna voltages. The Fourier coefficients (16) represent convenient intermediate data products because, as will be shown in Section III-B, they are readily expressed in terms of the radial current velocity.

Ideally, the averages indicated by angular brackets $\langle\cdots\rangle$ are infinite-ensemble averages. In practice we form a finite N-sample average of the various cospectra defined in (16). As shown in Appendix B, such cospectra can be averaged over N independent samples to reduce the fractional variance of their statistical fluctuations by a factor of N. The actual Gaussian voltages from the antennas cannot be averaged; this destroys information and does not reduce the fractional variance.

3) Data Covariance Matrix: We will now derive an expression for the covariance matrix of the Fourier coefficients which is required for the determination of statistical uncertainties in the current velocities. The complex voltages have real and imaginary components that are independent, zero-mean Gaussian random variables. Expressions for the probability density and covariance between cospectra $P_{\alpha\beta}$ and $P_{\gamma\delta}$ for an N-sample average are derived in Appendix B; the covariance is given by

$$\mathrm{Cov}\,({}_N P_{\alpha\beta}\,{}_N P_{\gamma\delta}) = \frac{1}{2N}(P_{\alpha\gamma}P_{\beta\delta} + P_{\alpha\delta}P_{\beta\gamma}). \tag{17}$$

The covariance matrix $C_{m,n}$ of the Fourier coefficients $b_n(\omega)$ follows from (15)-(17)

$$C_{m,n} = \frac{\pi^2}{2N}\begin{bmatrix} 4(P_{11}P_{22}+P_{12}^2) & 8(P_{12}P_{23}+P_{22}P_{13}) & 12P_{13}P_{23} & 8(P_{13}P_{12}+P_{11}P_{23}) & 4P_{12}(P_{11}-P_{12}) \\ 8(P_{12}P_{23}+P_{22}P_{13}) & 16(P_{22}P_{33}+P_{23}^2) & 24P_{23}P_{33} & 16(P_{13}P_{23}+P_{33}P_{12}) & 8(P_{12}P_{13}-P_{22}P_{23}) \\ 12P_{13}P_{23} & 24P_{23}P_{33} & 18P_{33}^2 & 24P_{13}P_{33} & 6(P_{13}^2-P_{23}^2) \\ 8(P_{13}P_{12}+P_{11}P_{23}) & 16(P_{13}P_{23}+P_{33}P_{12}) & 24P_{13}P_{33} & 16(P_{11}P_{33}+P_{13}^2) & 8(P_{11}P_{13}-P_{12}P_{23}) \\ 4P_{12}(P_{11}-P_{12}) & 8(P_{12}P_{13}-P_{22}P_{23}) & 6(P_{13}^2-P_{23}^2) & 8(P_{11}P_{13}-P_{12}P_{23}) & 2(P_{11}^2-2P_{12}^2+P_{22}^2) \end{bmatrix} \tag{18}$$

where $m, n = -2, -1, \cdots, 2$.

The cospectra are easily calculated from $b_n(\omega)$ using (16) and the identity

$$P_{11} + P_{22} = P_{33}. \tag{19}$$

Therefore, the data covariance matrix can be calculated from the N-sample averaged data values themselves.

B. Radial Current Velocity Maps

In order to obtain ocean surface parameters from the Fourier angular coefficients, they must be defined in terms of the narrow-beam radar cross section, which is related to ocean surface parameters in a well-established formulation [2].

Using the definition of the voltages in terms of the sea-echo return given in (1)-(3), (11) becomes

$$\tilde{\sigma}(\omega, \psi) = \left\langle \left| \frac{1}{2\gamma} \int_{-\gamma}^{\gamma} \cos^2\left(\frac{\psi - \phi}{2}\right) \mathring{g}(\phi)\, d\phi \right|^2 \right\rangle$$

$$= \frac{1}{2\gamma} \int_{-\gamma}^{\gamma} \cos^4\left(\frac{\psi - \phi}{2}\right) \sigma(\omega, \phi)\, d\phi \tag{20}$$

where the narrow-beam radar cross section $\sigma(\omega, \phi)$ is defined by (6). From (12) and (20) we obtain

$$b_n(\omega) = \frac{1}{\gamma \epsilon_n} \int_{-\gamma}^{\gamma} d\phi \int_{-\pi}^{\pi} d\psi \cdot \cos^4\left(\frac{\psi - \phi}{2}\right) \sigma(\omega, \phi) tf_n(\psi). \tag{21}$$

Expanding the cosine term in (21) as a trigonometric series gives

$$\cos^4\left(\frac{\psi - \phi}{2}\right) = \sum_{n=-2}^{2} q_n tf_n(\psi) tf_n(\phi) \tag{22}$$

where $q_{-2} = q_2 = 1/8; q_{-1} = q_1 = 1/2; q_0 = 3/8$.

Substituting this expansion into (21) and performing the integration gives the required expression for the Fourier angular coefficients in terms of the narrow-beam radar cross section

$$b_n(\omega) = \frac{q_n \pi}{\gamma} \int_{-\gamma}^{\gamma} \sigma(\omega, \phi) tf_n(\phi)\, d\phi. \tag{23}$$

Barrick's equation [2] for the first-order radar cross section in the absence of surface currents is given by

$$\sigma(\omega, \phi) = 2^6 \pi k_0^4 \sum_{m=\pm 1} S(-2m\tilde{k}_0) \delta(\omega - m\omega_B) \tag{24}$$

where $m = \pm 1$ denotes the sign of the Doppler shift, $\tilde{k}_0$ is the radar wave vector (of magnitude k_0 pointing toward the scattering patch at azimuth ϕ), and $S(\cdot)$ is the directional ocean waveheight spectrum. The Bragg resonance condition is imposed by the delta function constraint. Thus ideally for a *narrow-beam* radar, the first-order peaks are impulse functions at the Bragg frequencies ω_B defined in terms of the radar wavenumber by the dispersion equation

$$\omega_B = \sqrt{2gk_0} \tag{25}$$

where g is the gravitational acceleration. In the presence of a surface current, the peaks are Doppler-shifted in frequency by an amount $\delta\omega$ that is proportional to the radial current velocity $v(\phi)$ at the scattering patch

$$\delta\omega = 2k_0 v(\phi). \tag{26}$$

For example, at our radar frequency of 25.4 MHz, (25) gives a Bragg frequency $\omega_B/2\pi = 0.514$ Hz, corresponding to ~2-s or 6-m gravity waves; a current speed $v(\phi)$ in (26) of 50 cm/s would result in a frequency shift $\delta\omega/2\pi = 0.085$ Hz.

Inserting (24)-(26) into (23) gives the following equation:

$$b_n(\omega) = \frac{2^6 q_n \pi^2 k_0^4}{\gamma} \sum_{m=\pm 1} \int_{-\gamma}^{\gamma} S(-2m\tilde{k}_0) tf_n(\phi) \cdot \delta(\omega - m\omega_B - 2k_0 v(\phi))\, d\phi. \tag{27}$$

This equation expresses the data in the first-order region in terms of the radial current velocity occurring over a range cell of constant radius. The radial velocity is a function of azimuth; therefore, the first-order peak is not only displaced in frequency (as it is for a narrow beam), but is also broadened in frequency into a form that depends on the radial current velocity pattern. In the remainder of this section, it will be shown how to interpret the form of the peak through (27) to give the radial velocity pattern.

It follows from (27) that the Doppler shift from the positive and negative Bragg frequencies uniquely defines a value of the radial current velocity; interpretation of the data using least-squares methods yields the azimuth angles at which this velocity occurs. The exact method used depends on uniqueness properties of the function $v(\phi)$. We shall now identify two possible uniqueness conditions which are defined by a wide variety of surface current patterns, show how statistical inference may be applied to the data to select the relevant condition, and describe the method of solution in each case. Any text on data analysis (e.g., [18]-[20]) may be consulted for an introduction to least-squares estimation and statistical hypothesis testing.

1) One-Angle Solution: In this case, it is assumed that the velocity defined by a given Doppler frequency occurs at only one azimuth angle. This condition applies at the maximum velocity for *any* current pattern and at every velocity when a uniform current flows parallel to the coast. Application of the delta function constraint in (27) leads to the following equation:

$$b_n(\omega) = q_n p_1 tf_n(\phi_1) \tag{28}$$

with p_1 given by

$$p_1 = \left. \frac{2^6 \pi k_0^4 S(-2m\tilde{k}_0)}{\gamma\, |2k_0 \partial v(\phi)/\partial\phi|} \right|_{\phi_1} \tag{29}$$

where $S(-2m\tilde{k}_0)$ is a function of ϕ through $\tilde{k}_0$.

Thus p_1 is a function of ϕ_1 but is independent of the index n. At each Doppler shift (and hence velocity) (28) defines a set of five equations in two unknowns p_1 and ϕ_1. Estimates of these parameters and their standard deviations may be made by minimizing the sum of squared deviations between the data and the model given by

$$I = \sum_{n=-2}^{2} [b_n(\omega) - q_n p_1 tf_n(\phi_1)]^2. \tag{30}$$

Least-squares methods to effect this minimization are described in Appendix A. Equation (28) is nonlinear in ϕ_1; therefore a grid search over ϕ_1 is performed to find the value that minimizes (30); however, (28) is linear in p_1, a closed-form solution therefore exists for the optimum value of p_1 corresponding to any choice of ϕ_1 (A4). This procedure gives estimates of p_1, ϕ_1, and their standard deviations.

2) Two-Angle Solution: For this case it is assumed that a given radial velocity occurs at two azimuth angles. Use of the delta function constraint in (27) now reduces that equation to

$$b_n(\omega) = q_n[p_1 tf_n(\phi_1) + p_2 tf_n(\phi_2)] \tag{31}$$

i.e., a set of five equations in four unknowns p_1, ϕ_1, p_2, ϕ_2 at each value of Doppler frequency. Here p_1 is defined in (29) and p_2 has a similar definition at azimuth angle ϕ_2. We solve for the four parameters by minimizing the sum given by

$$I = \sum_{n=-2}^{2} [b_n(\omega) - q_n p_1 tf_n(\phi_1) - q_n p_2 tf_n(\phi_2)]^2. \tag{32}$$

This involves a grid search over the nonlinear parameters ϕ_1 and ϕ_2. Since (31) is linear in p_1 and p_2 closed-form expressions for their optimum values and standard deviations are provided at each choice of ϕ_1 and ϕ_2 by least-squares methods (see Appendix A), we denote these estimates at the optimum values of ϕ_1 and ϕ_2 as

$$p_1^* \pm \Delta p_1 \quad p_2^* \pm \Delta p_2. \tag{33}$$

Standard deviations in the angle estimates are also given.

3) Statistical Resolution of One- versus Two-Angle Solution: Because the number of parameters sought in the one-angle model is less, direct comparison between the least-squares residuals cannot be used to decide between the two solutions. Therefore, we perform the following statistical test to decide objectively between the two hypotheses. The two-angle solution is calculated first, as described above. For this to be valid, both p_1 and p_2 must be nonzero. Since the data is effectively Gaussian (by the central limit theorem and also discussion in Appendix B), one can be 95.4-percent confident of a nonzero solution for p_1 and p_2 if

$$p_1^* > 2\Delta p_1 \quad p_2^* > 2\Delta p_2. \tag{34}$$

If (34) is true, we accept the two-angle solution; otherwise it is rejected and the one-angle solution calculated and employed.

4) Statistical Uncertainties in Radial Velocities: The above procedure gives the azimuth angle as a function of radial velocity; this function must be inverted to give the radial velocity map. The optimum solutions for the angles ϕ_1 and ϕ_2 fall on a discrete grid of points selected for the least-squares grid search. (For example, in our analysis of ARSLOE data, we used a grid increment size of 5°.) Ideally, there would be a unique value of velocity corresponding to a given grid angle ϕ. However, because of noise and statistical fluctuation in the sea echo, there may be two or more values, which we will write as $v^i(\phi)$; in addition, combination of data from the positive and negative Bragg peaks will produce multiple values. When this happens we use standard statistical methods to combine the different velocities [19]. This gives the following optimum estimates of the current velocity $\bar{v}(\phi)$ and its standard deviation (or uncertainty) $\Delta\bar{v}(\phi)$ based on weighting in the averaging process by the individual uncertainties:

$$\bar{v}(\phi) = \left[\sum_i v^i(\phi)/(\Delta v^i(\phi))^2\right] \Big/ \left[\sum_i 1/(\Delta v^i(\phi))^2\right] \tag{35}$$

$$\Delta\bar{v}(\phi) = 1 \Big/ \sqrt{\sum_i 1/(\Delta v^i(\phi))^2}. \tag{36}$$

In these expressions, the individual velocity uncertainties $\Delta v^i(\phi)$ are obtained by error propagation (described in [20]) from the angular uncertainty $\Delta\phi$ that is given by the least-squares analysis:

$$\Delta v^i(\phi) = \frac{\partial v^i(\phi)}{\partial \phi}\,\Delta\phi. \tag{37}$$

This relationship is valid for small fluctuations and is easily derived by expanding $v^i(\phi)$ in a Taylor series and retaining only first-order terms. The slope (or transformation Jacobian) $\partial v^i(\phi)/\partial\phi$ is obtained by numerical differentiation and the angular uncertainty $\Delta\phi$ is obtained from the data using standard least-squares methods described in Appendix A.

The current velocity and its standard deviation given in (35) and (36) represent the optimum solution produced by minimizing the sums of squared deviations given by (30) and (32). For the solution with minimum variance, the quadratic form to be minimized should include multiplications by the covariance matrix inverse as described in Appendix A. In (30) and (32) terms in the sum are weighted equally; we did not multiply by the covariance matrix inverse because both theory and experimental data show it to be singular in the first-order region. Equal weights are generally used when the covariance matrix is singular or unknown. We are presently extending the standard techniques to handle singular covariance matrices.

C. Calculation of Total Current Velocities

The basic information provided by the radar system is a two-dimensional map of radial current velocity obtained using the methods described in Section III-B. One normally requires the total current velocity; we will now discuss how to get total velocity vectors from the radials. Three methods are described: in the first, radial velocities measured from two geographically

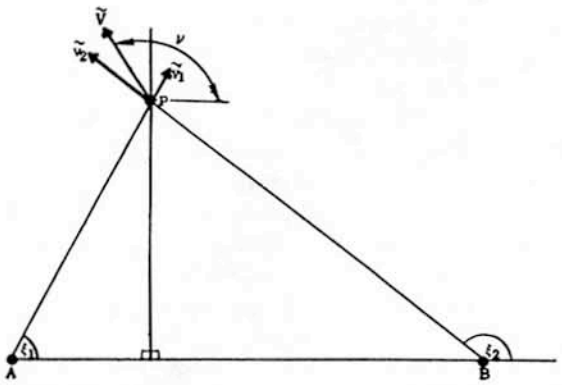

Fig. 5. Combination of radial current vectors $(\tilde{v}_1, \tilde{v}_2)$ measured from two radar sites A, B, at point P, defined by angles ξ_1 and ξ_2 with respect to the coast. The total current vector V is at angle ν with respect to the right coastline.

separated locations are combined to form a total vector. This method is free of assumptions on the current pattern, but the area that can be covered from two sites is often rather limited. The other methods may be applied when data from only one site is available. In one, a uniform current is assumed to flow over an extended region and the total vector obtained by fitting to the radials. In the other method, the equation of continuity is solved in the radar coverage area to give the azimuthal velocity components.

1) Combination of Data from Two Radar Sites: For two-site radar operation, the common coverage area is divided into area cells; radial velocities measured from the two sites that fall within a given area cell are interpreted to give a total current velocity. This situation is illustrated in Fig. 5, where radial vectors v_1, v_2 measured from the two sites are available at a given point P. This is not always the case, however; methods described below apply to an arbitrary number of radial velocities distributed anywhere in the cell.

In the remainder of this section, it will be convenient to define angles with respect to the right coastline, as in Fig. 5. We define the radial velocities, standard deviations, and corresponding azimuth angles within a given area cell measured from either radar site as v_i, Δv_i, ξ_i where $i = 1, 2, \cdots, N$. The radial velocities are expressed in terms of the total current velocity (defined to have magnitude V and direction ν) through the equation

$$v_i = V \cos (\nu - \xi_i). \tag{38}$$

When there are at least two radial vectors within the cell, estimates of V and ν can be determined from (38) by least-squares fitting to the data (v_i, ξ_i) by minimizing the sum of weighted deviations given by

$$I = \sum_{i=1}^{N} \frac{w_i [v_i - V \cos (\nu - \xi_i)]^2}{(\Delta v_i)^2}. \tag{39}$$

If $N < 2$, the problem is underdetermined; a gap may be left on the map at this location, indicating insufficient information, or a larger area cell can be used to include more radial vectors. For this problem we have included additional weighting factors w_i in the least-squares sum. For example, the weights could represent an area averaging or filtering process, or if the total current at a particular point within the area cell is desired, radial velocities could be weighted according to their Cartesian distance from the point, as in the Lagrange interpolation procedure. In this case, the weights w_i can be proven to be identically the Lagrange interpolating weights given in standard tables, (e.g., "Bivariate Interpolation", [29, section 25.2.65-67]. Because (38) is nonlinear in ν, we perform a grid search over this parameter to find the value that minimizes (39), with the optimum value of V for any choice of ν defined by

$$V = \frac{\sum_{i=1}^{N} w_i v_i \cos (\nu - \xi_i)/(\Delta v_i)^2}{\sum_{i=1}^{N} w_i \cos^2 (\nu - \xi_i)/(\Delta v_i)^2}. \tag{40}$$

The following closed-form expressions for the standard deviations in speed and direction can be derived using methods described in Appendix A:

$$\Delta V = \left\{ \frac{\sum_{i=1}^{N} w_i \sin^2 (\nu - \xi_i)/(\Delta v_i)^2}{\left| \sum_{i=1}^{N} \sum_{j=1}^{N} w_i w_j \sin (\xi_i - \xi_j)/(\Delta v_i \Delta v_j)^2 \right|} \right\}^{1/2} \tag{41}$$

$$\Delta \nu = \left\{ \frac{\sum_{i=1}^{N} w_i \cos^2 (\nu - \xi_i)/(\Delta v_i)^2}{V^2 \left| \sum_{i=1}^{N} \sum_{j=1}^{N} w_i w_j \sin (\xi_i - \xi_j)/(\Delta v_i \Delta v_j)^2 \right|} \right\}^{1/2}. \tag{42}$$

We now denote azimuth angles measured from the first and second radar sites as ξ_i^1 and ξ_i^2, respectively. For small area cells, the values of ξ_i^1 are approximately the same; therefore such pairs do not contribute significantly to the value of the double sum in the denominator of (41) and (42). The same applies to $\xi_i^2 - \xi_j^2$ and the sum is normally dominated by pairs from different sites. However, when the area cell lies close to the line joining the sites (where $\xi_i - \xi_j \cong 0, \pi$), all terms in the double summation become small and the corresponding uncertainties ΔV, $\Delta \nu$ are very large; this is often referred to as baseline instability [9], [16].

2) Model-Fitting Technique: In this technique, the current is assumed to be uniform in an extended spatial region, for example, in bands several kilometers in width parallel to the shoreline, if this model is believed to be representative of typical current flow in the given region. Estimates of the total current speed and direction, together with their uncertainties, are then obtained using least-squares methods, minimizing the sum of weighted deviations given in (39); however, in this case, i ranges over all points falling within the band and the weights w_i would normally be set to unity. There is the usual tradeoff between spatial resolution and uncertainty: the bands must be chosen to be wide enough that the statistical uncertainty is

sufficiently small; this may reduce small-scale current information.

3) Application of the Equation of Continuity: With this method, we determine the azimuthal velocity components from the radial components measured by the radar by solving the equation of continuity at the surface, ignoring the vertical water motion [30].

In order to apply the equation of continuity, it is convenient to express both radial and azimuthal components of the velocity at the jth cell at range r_j and at azimuth angle ξ as a Fourier series over angle

$$v_r(\xi) = \sum_{n=-N}^{N} R_n(r_j) tf_n(\xi) \tag{43}$$

$$v_\xi(\xi) = \sum_{n=-N}^{N} \Theta_n(r_j) tf_n(\xi) \tag{44}$$

where $v_r(\xi)$ and $v_\xi(\xi)$ are the radial and azimuthal components, respectively, and the angle ξ is defined with respect to the right coastline as in Fig. 5. The radial Fourier coefficients and their covariance matrix $C^R(r_j)$ are determined from the measured radial components using least-squares fitting and error propagation as described in Appendix A. The quantity to be minimized is the weighted sum of squared deviations given by

$$I = \sum_{i=1}^{M} \frac{\left[v_r(\xi_i) - \sum_{n=-N}^{N} R_n(r_j) tf_n(\xi_i) \right]^2}{(\Delta v_r(\xi_i))^2} \tag{45}$$

where the sum extends over the M available radial velocities in the range cell. Since the problem is linear in the coefficients $R_n(r_j)$, the optimum values which define the minimum value of I (i.e., I_{min}) are closed-form expressions.

Although there may be oceanographic reasons why a given number of angular harmonics are appropriate in (43) and (44), the first question to ask is how many terms in (43) *can* be fitted to noisy radial velocity data. With too few, the model (43) will not describe the data adequately; if too many are requested, the uncertainties in the derived coefficients will dramatically increase. An objective statistical method to determine the number of coefficients which should be included in the least-squares sum (45) is the χ^2 test [19]. Both I and I_{min} are χ^2-distributed; I has M degrees of freedom; if $(2N+1)$ Fourier coefficients are obtained by fitting, I_{min} has $(M-2N-1)$ degrees of freedom. When the fitting function (43) with N terms is a good approximation to the data, the value of $I_{min}/(M-2N-1)$ should be reasonably close to unity. If it is considerably larger, the deviations are too great, indicating that not enough terms have been included in the Fourier series expansion to fit the data adequately. To use the χ^2 test, a significance level α (usually small) is chosen and the value of I_{min} compared with the fractile $\chi^2_{(1-\alpha)}$ for $(M-2N-1)$ degrees of freedom. (Tables of $\chi^2_{(1-\alpha)}$ are available in the statistical texts [19] and [20].) The number of terms in the Fourier series should be increased until I_{min} is approximately equal to $\chi^2_{(1-\alpha)}$.

The azimuthal Fourier coefficients for nonzero n can be obtained by solving the equation of continuity, which is given in polar coordinates by

$$\frac{\partial v_\xi}{\partial \xi} = -\frac{\partial (r v_r(\xi))}{\partial r} \tag{46}$$

where the vertical sea-surface movement has been set to zero and the depth assumed to be constant.

Substitution of (43) and (44) into (46) gives for the jth range cell

$$\Theta_n(r_j) = \frac{-1}{n} \frac{\partial}{\partial r} (rR_{-n}(r))|_{r_j}, \qquad \text{for } n \neq 0. \tag{47}$$

For uniformly spaced range cells of width Δr, the range at the jth cell can be written

$$r_j = j\Delta r. \tag{48}$$

The differentiation in (47) can be performed numerically to give

$$\Theta_n(r_j) = -\frac{1}{2n} \left[(j+1)R_{-n}(r_{j+1}) - (j-1)R_{-n}(r_{j-1}) \right]. \tag{49}$$

The covariance matrix of the azimuthal components follows from the radial covariance matrix $C^R(r_j)$ using (49). Since we have established that the radial components in different range cells are essentially uncorrelated, the (m, n)th element can be written

$$C_{m,n}^{\Theta} = \frac{1}{4mn} \left[(j+1)^2 C_{-m,-n}^{R}(r_{j+1}) + (j-1)^2 C_{-m,-n}^{R}(r_{j-1}) \right]. \tag{50}$$

The zero-order coefficient $\Theta_0(r_j)$ is a constant of integration of the differential equation (46), and follows from the boundary condition that the normal velocity component $v_\xi(\xi)$ must be zero at the coastline ($\xi = 0, \pi$). The first-order differential equation allows for the use of one boundary condition, although there are two boundaries that physically require zero normal flow. Satisfaction of the condition at one boundary (e.g., $\xi = 0$) does *not*, in general, guarantee satisfaction at the other ($\xi = \pi$). There are several possible ways to deal with this problem:

a) determine $\Theta_0(r_j)$ required for each boundary separately and average the two;

b) enforce the constraint (in a least-squares sense) that $v_\xi^2(\xi)$ described by (44) be minimized over land ($\pi < \xi < 2\pi$); or

c) choose either a coordinate system or a current representation over land such that both boundary conditions are automatically satisfied.

It can be shown that a) is identical to b) for arbitrary current patterns; we will examine formulations that invoke c).

We will now outline three methods for the detailed application of these equations. These methods differ in the type of Fourier expansion used and in the current velocity assumed over land, which is arbitrary.

Method A: In this method, the Fourier expansions in (43) and (44) are taken over all integer values of n such that $|n| < N$. For a stable determination of the Fourier coefficients, we must have $v_r(\xi)$ defined over the total angular range $0 < \xi < 2\pi$, since the basis functions are orthogonal and complete over this range. If one attempts to fit to the radial velocities over the half-plane defined by sea only ($0 < \xi < \pi$), the uncertainties in the derived parameters will be unacceptably large. In this method, we take the radial velocity to be zero over the land ($\pi < \xi < 2\pi$).

Boundary conditions as outlined in a) and b) for the azimuthal component $v_\xi(\xi)$ both give the same result for $\Theta_0(r_j)$:

$$\Theta_0(r_j) = -\frac{1}{\pi}\int_0^{2\pi}\left[\sum_{n\neq 0}\Theta_n(r_j)tf_n(\xi)\right]d\xi = \frac{2}{\pi}\sum_{n=1,3,5,\cdots}\frac{\Theta_{-n}(r_j)}{n}. \tag{51}$$

The covariance matrix elements containing the zero element follow from (51)

$$C_{0,m}^{\Theta}(r_j) = C_{m,0}^{\Theta}(r_j) = \frac{2}{\pi}\sum_{n=1,3,\cdots,N}\frac{C_{m,-n}^{\Theta}(r_j)}{n} \quad \text{for } m \neq 0$$

$$C_{0,0}^{\Theta}(r_j) = \frac{2}{\pi}\sum_{m=1,3,\cdots,N}\sum_{n=1,3,\cdots,N}\frac{C_{-m,-n}^{\Theta}(r_j)}{mn}. \tag{52}$$

Method B: In an alternative treatment of the velocity pattern over land, we "reflect" the velocity about the coast, i.e., make it an even function of ξ such that $v_r(\xi) = v_r(-\xi)$. It follows that the Fourier series (43) and (44) will contain only cosine and sine terms, respectively. Therefore, the azimuthal velocity component is automatically zero at the coast ($\xi = 0, \pi$) as required physically. Similarly, the zero-order azimuthal Fourier coefficient is zero.

Method C: Here we expand the current fields in a set of trigonometric basis functions that is orthogonal and complete over the range $0 < \xi < \pi$, by retaining only even values of n in (42) and (44), i.e., $-N, \cdots, -4, -2, 0, 2, 4, \cdots, N$. The coefficients of the modified series (43) can then be determined stably by fitting to the measured radial velocity over the sea surface. The condition that $v_\xi(\xi)$ be zero along the coast (which is now one and the same boundary in this coordinate system) gives the following expression for the zero-order coefficient:

$$\Theta_0(r_j) = -\sum_{n=1,2,\cdots,N}\Theta_{2n}(r_j). \tag{53}$$

The covariance matrix elements containing the zero element are defined by

$$C_{0,2m}^{\Theta}(r_j) = C_{2m,0}^{\Theta}(r_j) = -\sum_{n=1}^{N} C_{2m,2n}^{\Theta}(r_j), \quad \text{for } m \neq 0$$

$$C_{0,0}^{\Theta}(r_j) = \sum_{m=1}^{N}\sum_{n=1}^{N} C_{2m,2n}^{\Theta}(r_j). \tag{54}$$

Whichever of these methods is used, the number of terms in the Fourier series expansion must be increased until the χ^2 test is obeyed. On the other hand, statistical uncertainty in the derived parameters increases with the number of terms fitted, because we are seeking more information from the same data set.

The radial and azimuthal velocity components at a given range and azimuth can then be calculated from (43) and (44). It can be seen from these formulas that the standard deviations in $v_r(\xi)$ and $v_\xi(\xi)$ are given by

$$\Delta v_r(\xi) = \sqrt{\sum_{m=-N}^{N}\sum_{n=-N}^{N} C_{m,n}^{R}(r_j)tf_m(\xi)tf_n(\xi)}$$

$$\Delta v_\xi(\xi) = \sqrt{\sum_{m=-N}^{N}\sum_{n=-N}^{N} C_{m,n}^{\Theta}(r_j)tf_m(\xi)tf_n(\xi)} \tag{55}$$

and that $v_r(\xi)$ and $v_\xi(\xi)$ are uncorrelated, because the $\theta_n(r_j)$ are calculated using data from adjoining range cells. The total velocity, of magnitude V and direction ν, is obtained by combining $v_r(\xi)$ and $v_\xi(\xi)$

$$V = \sqrt{v_r^2(\xi) + v_\xi^2(\xi)}$$

$$\nu = \xi + \tan^{-1}\left[v_\xi(\xi)/v_r(\xi)\right] \tag{56}$$

with standard deviations given by linear error propagation

$$\Delta V = \frac{1}{V}\sqrt{[v_r(\xi)\Delta v_r(\xi)]^2 + [v_\xi(\xi)\Delta v_\xi(\xi)]^2} \tag{57}$$

$$\Delta\nu = \frac{1}{V^2}\sqrt{[v_r(\xi)\Delta v_\xi(\xi)]^2 + [v_\xi(\xi)\Delta v_r(\xi)]^2}. \tag{58}$$

Of the three methods outlined above, the one that produces the lowest values of the uncertainties ΔV, $\Delta\nu$ should be used. In our analysis of ARSLOE data we found this to be Method A. Another of these methods might prove superior for a different coastline angle, or for operation from a platform.

IV. APPLICATION OF ANALYSIS TECHNIQUES TO ARSLOE DATA

The ARSLOE experiment was held in October and November, 1980, near Duck in North Carolina. The CODAR system was operated in a research mode for a period of two months taking measurements of waves and currents. We report here on the analysis of the most interesting portion of this data set to give ocean surface current maps; from October 23 to October 26, a storm front passed the area, causing complete wind reversal and leading to complex current conditions. The radar

TABLE I
DATA RUNS DURING THE ARSLOE EXPERIMENT

Run	Time (GMT)
1	October 22 1130
2	2330
3	October 23 0010
4	0515
5	0555
6	0915
7	1130
8	1330
9	1530
10	1730
11	2130
12	2330
13	October 24 0130
14	0330
15	0530
16	0730
17	0930
18	1130
19	1330
20	October 25 0920
21	0958
22	1036
23	1130
24	1230
25	1330
26	1628
27	1730
28	1951
29	2030
30	2320
31	October 26 0016
32	0130
33	0330
34	0530
35	0730

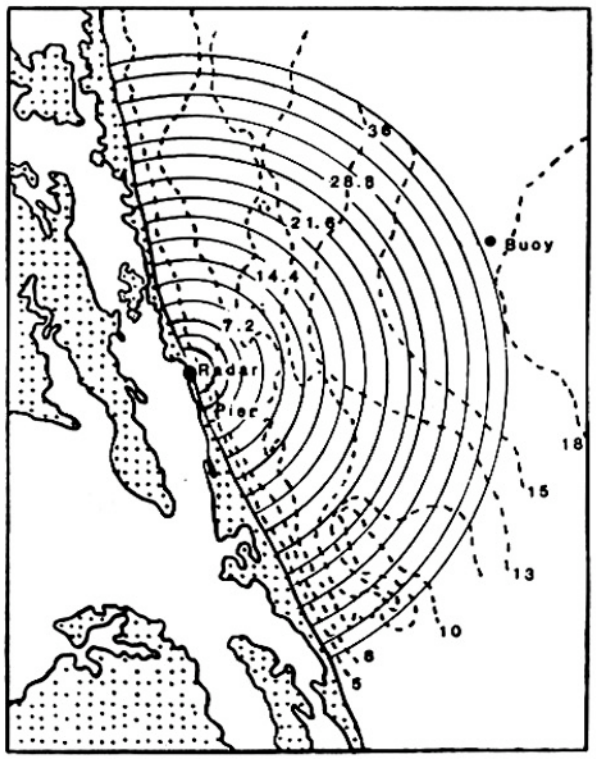

Fig. 6. The experimental configuration at ARSLOE. Radar range cells are indicated by circles, the depth contours by dashed lines.

was operated throughout the storm, with the exception of an 18-h gap when the system malfunctioned due to water in one of the cables. Data were collected during 35 runs, each lasting 36 min (Table I). The CODAR site was located about 3 km north of the CERC pier (Fig. 6). Radar data were taken from 30 range cells, each of 1.2-km extent, with a radar transmitter frequency of 25.4 MHz. In this section, we give details of the application of theoretical methods outlined in the previous section to the experimental data set and give examples of current velocity maps obtained. Section IV-A describes the initial data analysis that produced the voltage conjugate products, gives results of a statistical analysis of these quantities, and details the method that was applied automatically to separate the first-order spectrum from the surrounding continuum. Section IV-B describes the calculation of radial current velocities, gives examples of current maps obtained, and tabulates the statistical uncertainties obtained as a function of range and azimuth. Section IV-C describes the calculation of total current vectors and their uncertainties from model fitting and use of the equation of continuity and shows maps of current flow patterns throughout the storm. Uncertainties in current speed and direction are tabulated and the current and wind velocities compared. Section IV-D gives a general description of the current patterns observed during the storm.

A. Initial Data Analysis

1) Spectral and Statistical Analysis: The complex voltage time series from the three antennas were transformed using a four-sample Blackman-Harris window; this reduces sidelobes by 92 dB from the main lobe maximum, but destroys frequency resolution by a factor of two. This sidelobe suppression is included in the initial data analysis because it is essential to the derivation of the wave-height spectrum from the weaker higher-order echo. Fifteen 4.5-min time series were overlapped by 50 percent to give a total run time of 36 min. The correlation between consecutive spectra resulting from this overlap is theoretically only 4 percent [25]. Therefore, employing only every other frequency point in the output spectrum, we end up with the same frequency resolution as for nonoverlapped, rectangular-windowed time series segments of half the length, with the same number of statistically independent samples for subsequent averaging. We have thus reduced the sidelobe levels drastically, at the cost of calculating longer Fourier transforms. Time and spatial sampling resolution were 0.26 s and 1.2 km, respectively.

Before spectral averaging, we performed a detailed statistical analysis of spectra obtained from two data runs–October 24, 05:30 GMT (Run 15) and October 25, 16:28 GMT (Run 26). Details of these calculations are given in Appendix C. Correlation coefficients were calculated as a function of time, range, and frequency. This information is required for the estimation of the number of independent samples present in a composite spectrum obtained by averaging. From the results, we conclude the following.

1) The correlation between adjacent spectral power points (i.e., squared voltages) is about 60 percent; at greater frequency separation the correlation is not statistically significant.

2) Correlation between spectra obtained from the 50-percent overlapping time series is not statistically significant.

3) Correlation between spectra in adjacent range cells is

about 20 percent due to pulse stretching in the receiver; at greater range-cell separations, the correlation is negligible.

We also calculated the number of degrees of freedom per power spectral point as a check on the theory. Theoretically, the voltages are complex zero-mean Gaussian random variables; spectral powers should therefore be χ^2 variables with two degrees of freedom, where "degrees of freedom" is defined to be the inverse of the fractional variance. In reality, the voltages are not truly Gaussian, because the tails of the distributions eventually cut to zero, whereas Gaussian tails extend to infinity; this results in the observed number of degrees of freedom exceeding two; in our calculations (Appendix C) we obtained averaged results of 2.7 and 2.8 for the two runs.

2) Spectral Averaging: Because of the correlation (or statistical dependence) between adjacent frequencies, adjacent pairs in the spectrum were averaged; in addition, adjacent range cells were averaged to further reduce the statistical fluctuation in the composite spectrum. The resulting range and frequency resolutions, were 2.4 km and 0.00745 Hz. After averaging the 15 spectra from overlapping time segments, the number of sample averages was 30; thus an estimate of the covariance matrix of the data is given by (18) with $N = 30$.

3) Separation of the First-Order Spectrum: The composite spectra were then analyzed to isolate the first-order region of the spectrum from the surrounding continuum. The latter is due to higher order scatter from ocean waves and additive noise which can dominate in the more distant range cells where the higher-order echo is weaker. This separation is required because the theory described in Section III for obtaining current velocities applies only to the first-order region. The current velocity is proportional to the frequency shfit from the Bragg frequency; therefore the definition of the boundaries of the first-order regions is *very* important as they define the largest velocities. If the boundaries are set too wide, so that second-order echo is included and erroneously interpreted as first-order, not only will the azimuth angles associated with these spectral points be meaningless, but more important, the radial velocities inferred from them and erroneously attributed to currents will be far too large, totally biasing the entire current map. If one must err in setting these boundaries, they should be set too narrow, for this will simply result in gaps in the map (indicating no available data). We developed a set of general criteria which were applied automatically to isolate the first-order region for the ARSLOE date. These rules, described in detail in Appendix D, are based in part on the fact that the transition between the first- and second-order spectrum is extremely sharp; the increment of maximum magnitude between successive points in the spectrum (expressed in decibels) is used to define the boundary. In addition, no data is accepted that is less than ten times the noise at the edges of a ±1-Hz window surrounding the carrier frequency, where the sea echo is negligible. Examples of the separation produced by this automatic procedure are given in Fig. 7. The extent of the first-order region analyzed to give current velocities clearly depends both on the maximum current velocity and the signal power, and varies with both time and range. Thus the claim of Leise [16] that the limits of the first-order region need be set only once for any experiment is demonstrably incorrect. In our analysis, the procedure to isolate the first-order region is applied independently for positive and negative Doppler shift, for each range cell, and for every data run.

B. Radial Current Maps

We then produced maps of radial current velocities and their statistical uncertainties from the first-order spectra. The first step is the calculation of the azimuth angle corresponding to a given current velocity, using the basic methods described in Section III; however, we also included in the representations several models for additive noise; that which best fit the data was a nondirectional noise component (Δ). Thus the models (28) and (31) for the one- and two-angle solutions were replaced by

$$b_n(\omega)/q_n = p_1 tf_n(\phi_1) + \Delta\delta_n{}^0 \tag{59}$$

$$b_n(\omega)/q_n = p_1 tf_n(\phi_1) + p_2 tf_n(\phi_2) + \Delta\delta_n{}^0 \tag{60}$$

where $\delta_n{}^0$ is the Kronecker delta function and we estimated the noise term Δ, together with the angles and multiplicative factors, by least-squares fitting to the data. This additional noise parameter was found to be small but statistically significant; its inclusion improves the model-fit to the data without significantly affecting the results for current velocity.

The present calculation of a radial current map from echo spectra for a 36-min run takes about 10 min on a PDP 11/23 microcomputer for current velocities of the order of ±40 cm/s. Coded in Fortran, we have as yet made no attempt to speed up the program for operational use. Even at its present speed, this portion of the calculation can be considered "real time" in relation to the data-acquisition time.

The intrinsic statistical uncertainty in the resulting estimates of azimuth angle due to data fluctuations is typically between 1° and 3°. This can be compared with 10° estimates of uncertainty made by Leise [16] for the NOAA 4-element system; this difference is no doubt due to different analysis techniques. The grid increment should be chosen so that its contribution to the total uncertainty is small. Our results for the intrinsic angular uncertainty led to the choice of a grid spacing of 5°. The uncertainty (or quantization noise) due to the finite grid spacing was estimated as follows: the variance ϵ^2 arising from a uniform distribution of points falling within the grid spacing μ is given by

$$\epsilon^2 = \frac{1}{\mu}\int_0^{\mu/2} \theta^2\, d\theta = \frac{\mu^2}{12}. \tag{61}$$

This quantity was added to the variance due to the statistical fluctuation in the data (i.e., the square of the intrinsic statistical uncertainty discussed at the start of this paragraph). The standard deviation in angle $\Delta\phi$ is then the square root of the total variance and uncertainties in velocity follow from those in angle as explained in the previous section. Table II presents the mean uncertainty in velocity taken over 30 angular sectors,

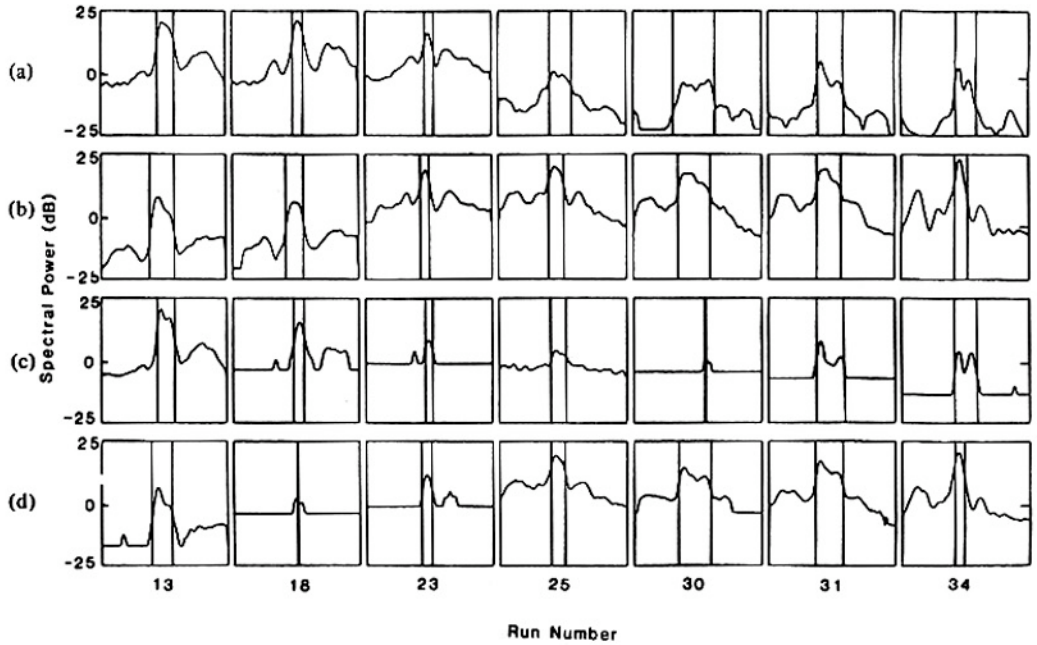

Fig. 7. Examples of the separation of the first-order region used to give current velocities, which lies between the vertical lines. The four spectra in a vertical column have the same run number, indicated below, with corresponding times given in Table I. Rows of spectra are as follows: (a) positive Doppler, range 12 km; (b) negative Doppler, range 12 km; (c) positive Doppler, range 24 km; (d) negative Doppler, range 24 km. Positive Doppler frequency ranges from 0.2 to 0.8 Hz; negative from −0.8 Hz to −0.2 Hz. ("Noise" level that appears flat has been artificially set to a threshold 6 dB above the noise at the edges of the spectral window.)

TABLE II
MEAN STANDARD DEVIATIONS IN RADIAL VELOCITY

Range (km)	Standard Deviation (cm/s)					
	0-30°	30-60°	60-90°	90-120°	120-150°	150-180°
2.4	2.7	1.7	2.1	2.4	2.8	6.4
4.8	5.4	2.3	2.2	2.3	2.6	3.8
7.2	4.1	2.2	2.2	3.3	1.9	3.4
9.6	4.4	2.6	2.8	2.6	2.1	4.3
12.0	4.2	2.2	2.4	3.0	2.6	3.2
14.4	3.6	2.2	2.2	2.8	3.1	6.8
16.8	3.3	2.2	2.2	2.7	3.1	5.1
19.2	3.7	2.2	2.7	2.2	2.5	5.6
21.6	4.3	2.3	2.0	2.3	3.0	3.4
24.0	4.3	2.5	2.7	2.7	3.1	5.4
26.4	4.7	2.7	2.5	3.3	3.3	5.9
28.8	2.6	3.4	2.4	2.4	3.3	10.8
31.2	8.7	2.8	2.2	2.6	3.1	13.5
33.6	3.3	2.6	2.4	2.8	2.9	7.2
36.0	8.7	4.1	2.2	2.2	3.1	7.2

averaged over the 35 data runs. The velocity uncertainty is greatest (typically 4-10 cm/s) in angular sectors close to shore (0°-30°, 150°-180°), because these sectors contain relatively few data points, due to low signal power resulting from coastline refraction and attenuation effects. In the remaining angular range (30°-150°), the statistical uncertainty is between 2 and 3.5 cm/s.

Examples of radial current velocity maps and the associated standard deviations are given in Figs. 8, 9, and 10. The largest gaps in the coverage occur in the sectors near the coast; this is explained by the facts that a) radar refraction near grazing to a coast can place the apparent bearing of the signal several degrees out to sea, and b) signal attenuation is considerably greater at angles grazing the coast.

C. Total Current Vectors

1) Model Fitting: Using the method described in Section III-C2) we assumed that a uniform current was flowing in a set of strips parallel to shore and obtained the total current speed and direction by least-squares fitting to the radial velocities. Results for the total current vectors are shown in Fig. 11. Uncertainties in current speed and direction are given as a function of range in Table III. The width of the bands was chosen to increase with distance to compensate for the decreasing number of data points resulting from the loss of power with range. In fact, we overcompensated for this effect; the uncertainties actually *decrease* with range. The sum of squared deviations between the fitted model and the data were too large (by about a factor of two) to obey the χ^2 test, because of inhomogeneity within the strips. Inclusion of more parameters in the model to describe the inhomogeneity would have provided a better fit to the data; however, a condensed interpretation is produced by "forcing" an average over distance along the shore. Note that the standard deviations listed in Table III correspond to statistical uncertainties in the data; the low values indicate that the "forced" average is stable with respect to data fluctuations. We have not estimated bias in the results due to the inadequacy of the model fit.

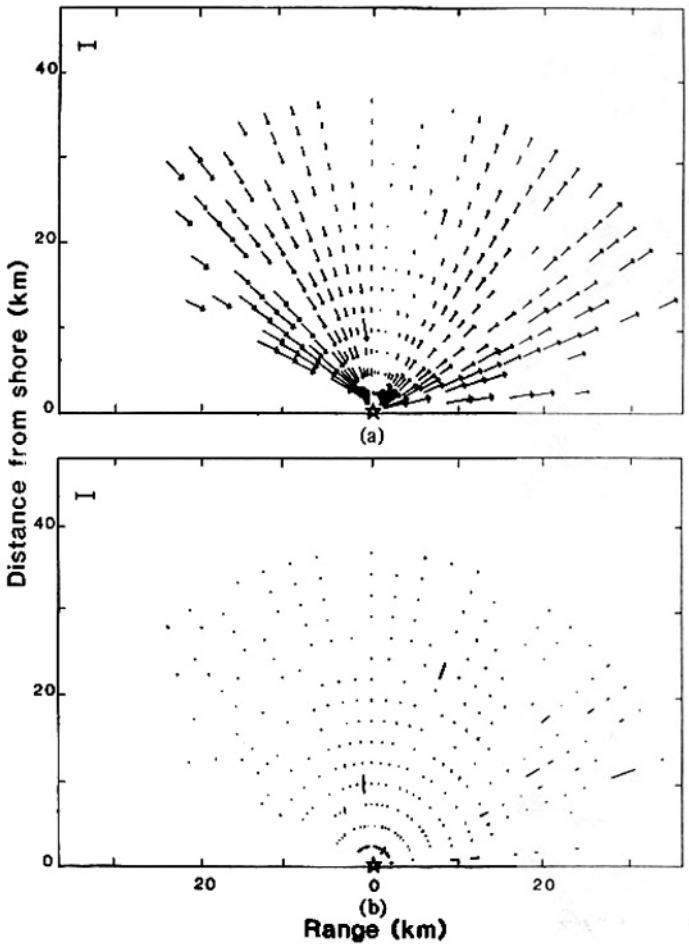

Fig. 8. (a) Radial current vectors for Run 13 (October 24, 0130Z). The length of each arrow is proportional to the radial velocity; the bar in the upper left corresponds to 20 cm/s. (b) 95.4 percent confidence intervals ($\pm 2\sigma$) for the radial current vectors.

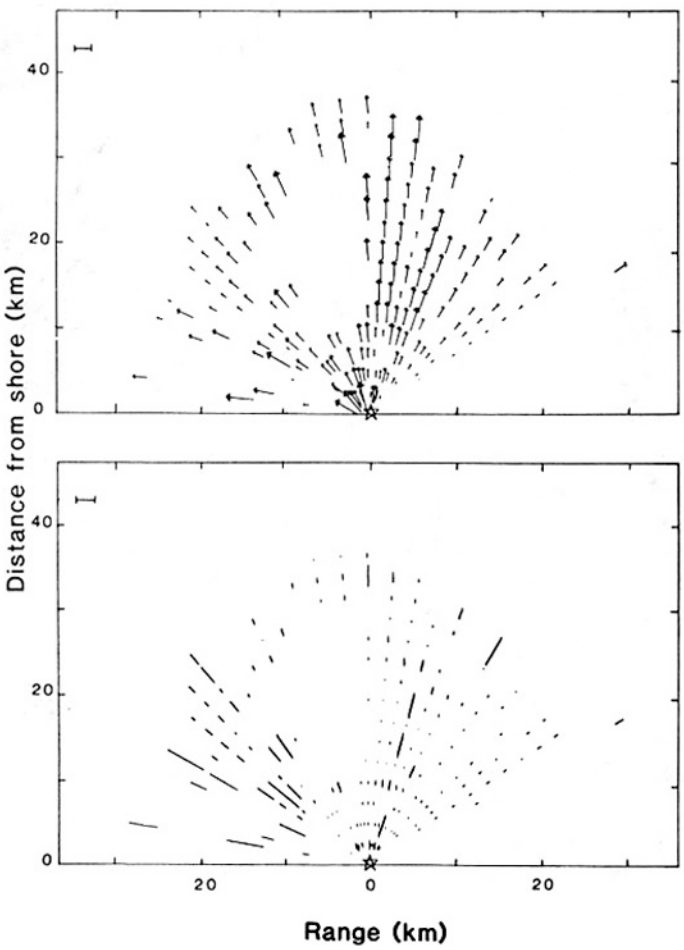

Fig. 9. As for Fig. 8: Run 26 (October 25, 1628GMT).

Before the start of the storm, current flowed northward along the coast. As the northerly storm winds started to blow, the current flow turned south and increased in speed, until the wind reversed, causing a complete reversal in the current direction. The general direction of the current observed by CODAR was verified by the motion of dye samples dropped from the end of the CERC pier, which indicated if the flow was northward or southward [31]. Fig. 12 shows a comparison between current speed and direction (at 8-km range) and that of the wind, for October 23-25. The wind was measured at the XERB buoy which was located 37 km out from the pier (Fig. 6). Current and wind direction are highly correlated and the average current speed throughout the period was 2.1 percent that of the wind. CODAR senses the current in the upper meter of the ocean, somewhat deeper than the direct wind-driven current; therefore wind/current correlations may not always be high.

2) Application of the Equation of Continuity

Using the methods described in Section III-C3, we applied the equation of continuity to derive the total velocity vectors; the Fourier angular coefficients of the radial velocity in each range cell were first derived by fitting to the available radial vectors and the azimuthal components then obtained by solving the equation. Methods A, B, and C were applied, the number of terms in the Fourier series (43) and (44) being increased until the χ^2 test was obeyed. We then compared the resulting uncertainties in the total velocities; these did not differ markedly, but Method A in general gave the lowest uncertainties. We therefore present the results given by application of this method, which was found in the majority of cases to require nine Fourier coefficients in order to satisfy the χ^2 test (i.e., up through the fourth harmonic). Maps of total current velocity, corresponding to the radial maps of Figs. 8, 9, and 10 are given in Fig. 13.

Table IV gives standard deviations in current speed and angle, obtained in 30° angular sectors and averaged over the 35 runs. Uncertainties in the total velocities depend both on the uncertainties in the input radial data and its angular extent. Gaps in the angular coverage, the largest of which occurs at the coast (see Section IV-B) decrease the accuracy of the total velocity estimate over the whole range cell. The coastal gap is larger at the more distant range cells where the signal/noise ratio is less, the observed radial velocities tending to cluster in the region of maximum signal strength. This causes

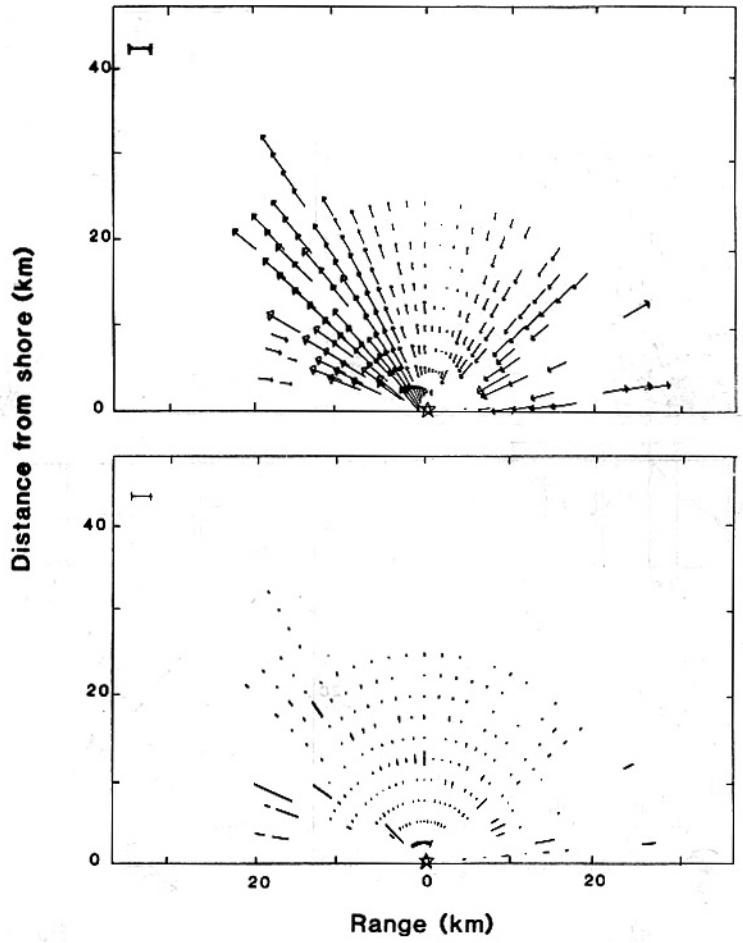

Fig. 10. As for Fig. 8: Run 30 (October 25, 23:20 GMT).

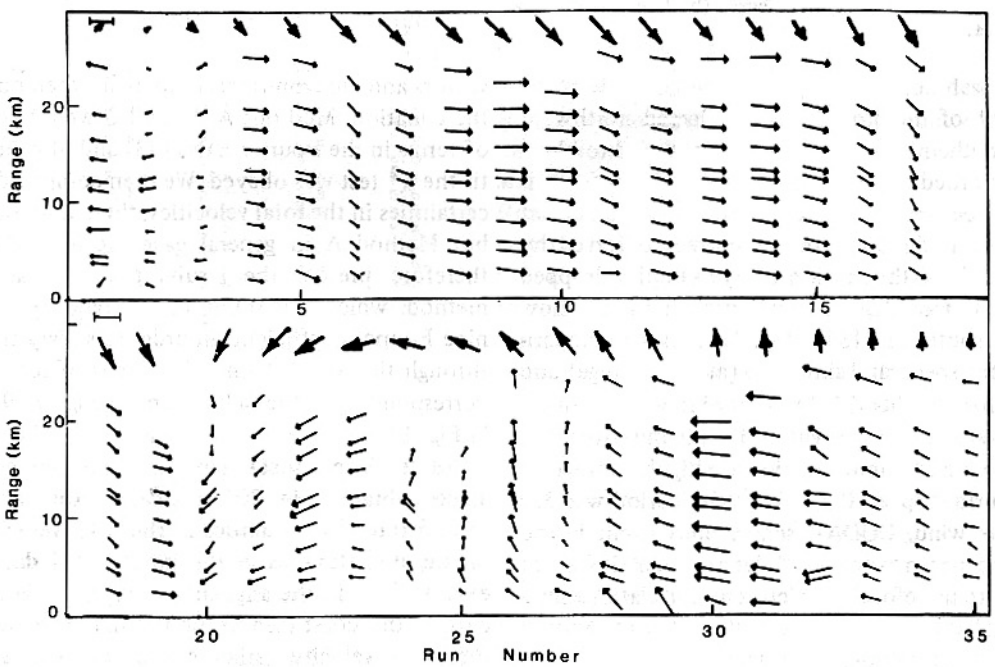

Fig. 11. Total current vectors plotted versus range for the 35 ARSLOE runs. The run number is indicated; corresponding times are listed in Table I. The length of each vector is proportional to the current speed; the bar in the upper left corresponds to 20 cm/s. The bold arrows represent the wind vectors (length is proportional to windspeed).

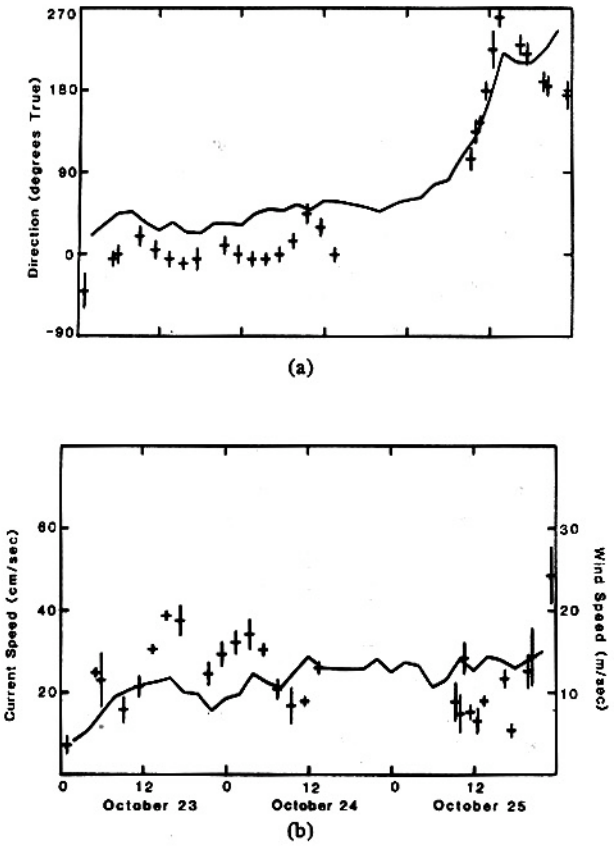

Fig. 12. (a) Comparison between current and wind direction. (b) Comparison between current and windspeed. Total current vectors measured by CODAR 8 km from shore (plotted as points with $\pm 1\sigma$ standard error bars). Wind measured at the XERB buoy (plotted as a continuous line).

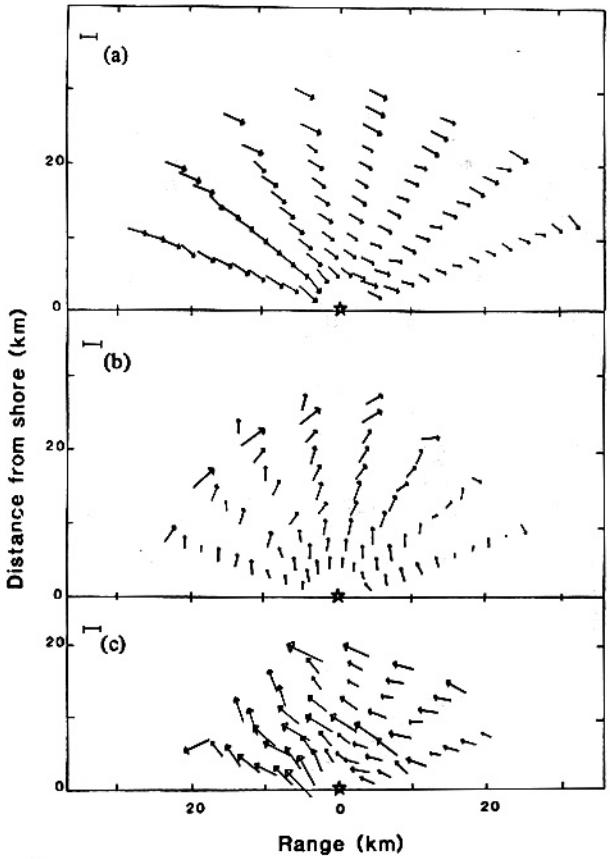

Fig. 13. Total current vector maps obtained using the equation of continuity. Times are the same as for the radial maps in Figs. 8-10: (a) October 24, 01:30 GMT (b) October 25, 16:28 GMT (c) October 25, 23:20 GMT. The length of each arrow is proportional to the current speed; the bar in the upper left corresponds to 20 cm/s.

TABLE III
MEAN STANDARD DEVIATIONS IN VELOCITY FROM MODEL FIT

Range (km)	Resolution (km)	V (cm/s)	ν (degrees)
1.8	0.9	5.5	20
4.8	1.2	3.9	13
6.0	2.4	4.1	13
8.4	2.4	3.2	10
10.8	2.4	3.4	12
13.2	2.4	4.5	11
14.4	3.6	4.5	11
16.8	3.6	3.8	11
19.2	3.6	3.6	11
21.6	3.6	4.0	10
28.3	8.2	2.7	8

the uncertainty in total velocity to increase as a function of range.

In Table V, we compare results for total current speed and direction obtained straight out from shore at a range of 9.6 km with the two methods, giving the standard deviation in each case. Results of the comparison are fair, considering that the model fit did not satisfy the χ^2 test: inhomogeneity within the strips parallel to shore is in fact demonstrated by the current maps produced using the equation of continuity (e.g., Fig. 13).

TABLE IV
MEAN STANDARD DEVIATIONS IN VELOCITY FROM THE EQUATION OF CONTINUITY

Range (km)	Standard Deviation in Speed (cm/s)					
	0-30°	30-60°	60-90°	90-120°	120-150°	150-180°
4.8	6.2	6.6	6.7	5.3	3.9	4.7
7.2	4.2	6.0	6.2	4.8	3.4	3.3
9.6	7.0	5.1	4.1	3.5	3.5	3.6
12.0	7.6	11.5	12.4	9.6	6.8	4.6
14.4	11.7	14.9	14.6	11.5	8.6	5.2
16.8	19.4	29.3	26.4	22.1	15.0	8.3
19.2	14.0	20.0	20.6	14.8	9.2	5.7
21.6	9.7	13.8	13.9	11.9	11.0	6.8
24.0	9.9	16.3	16.5	14.6	13.7	8.3
26.4	10.9	19.7	20.1	21.3	20.8	13.5
28.8	11.4	21.2	21.1	20.4	22.4	15.4
31.2	9.5	14.4	20.6	27.8	31.3	19.8
33.6	13.0	22.5	30.8	40.9	44.8	24.0

Range (km)	Standard Deviation in Angle (degrees)					
4.8	28	20	24	18	8	13
7.2	13	14	13	10	7	9
9.6	17	12	14	9	8	9
12.0	21	23	16	13	10	14
14.4	35	23	39	24	16	14
16.8	24	32	33	19	15	16
19.2	35	30	25	16	12	12
21.6	27	23	23	12	14	18
24.0	22	22	19	13	15	15
26.4	23	37	21	19	23	26
28.8	24	41	33	29	41	39
31.2	43	19	16	16	24	24
33.6	26	29	25	26	33	28

TABLE V
COMPARISON BETWEEN MODEL FIT AND EQUATION OF CONTINUITY AT 9.6 km

Run	Speed (cm/s)		Angle (degrees True)	
	Model	Equation	Model	Equation
1	26±37	12±6	175±44	226±31
2	20±5	7±4	155±10	215±28
3	5±2	10±5	-55±26	145±31
4	25±1	29±3	-5±7	9±6
5	25±1	67±22	0±6	-1±20
6	17±10	20±2	25±40	72±5
7	22±2	19±2	5±9	22±7
8	32±1	28±2	-10±6	11±2
9	40±2	41±3	-10±8	6±4
10	37±1	39±2	-5±5	11±2
11	26±2	23±3	10±7	31±8
12	29±2	21±1	0±13	31±4
13	31±6	24±1	-5±10	15±3
14	35±.4	26±1	-10±6	17±3
15	32±.6	21±1	0±6	32±3
16	21±1	17±2	20±8	68±5
17	17±2	5±2	50±10	108±26
18	18±1	19±2	30±10	39±5
19	22±10	24±1	0±8	15±3
20	29±6	38±8	120±8	151±13
21	15±5	30±16	120±10	156±31
22	30±4	58±6	145±8	165±6
23	19±3	32±2	160±9	160±3
24	24±2	16±1	210±12	266±3
25	18±1	17±2	265±9	273±5
26	27±2	25±1	240±12	260±2
27	14±1	13±1	230±10	258±4
28	22±3	35±4	200±9	-52±7
29	27±4	46±6	185±10	-29±8
30	52±20	53±12	170±13	190±10
31	36±4	17±1	175±14	226±5
32	31±3	7±3	180±20	215±28
33	27±1	41±1	190±7	191±2
34	19±5	14±2	205±38	234±7
35	21±3	31±2	175±5	187±4

D. Current Patterns Observed During the ARSLOE Storm

Surface currents measured under the rather complex storm at ARSLOE showed several interesting features. The current velocities varied little with distance from shore, suggesting that storm winds, currents, and wave fields were reasonably homogeneous over 40-km extents along this straight section of coast. Before and after the storm, the normal surface flow in this area is South to North, nearly parallel to the coast as shown by daily measurements of dye movement [31]. Tidal currents in this area are less than 5 cm/s. During strong, veering storm winds, surface currents followed the winds reasonably closely, responding almost immediately to wind direction changes. When the wind blew for a considerable period at an angle to shore, however, flow at the surface became more parallel to the coast. This is especially evident for the period from 05:30 GMT October 23 to 07:30 GMT October 24; the wind stayed at 0:40 T; while the currents were from 0:00 T (3:40 T is parallel to shore). Hence, only a slight angle to the coast is maintained by the current as the water level at the beach was observed to rise steadily over this period in the usual manner of a storm surge. As the wind veered from the Southeast through the South on October 25, the removal of the onshore stress caused an "overshoot," in which the surface current moved directly offshore, rapidly lowering the water level on the beach built up by the surge. Later, as the wind blew fairly strongly from the Southwest, the current aligned itself nearly parallel to shore from the South; as the wind intensity died, the parallel direction was maintained but the current speed dropped back to around 20 cm/s.

V. CONCLUSIONS AND RECOMMENDATIONS

A. Uncertainties in CODAR Measurements of Current Velocity

1) Statistical Uncertainties: Applied to ARSLOE data to a range of 36 km under a wide range of current conditions, least-squares methods estimate the angle at each radial velocity with typical rms uncertainties between 1° and 3° for a 36-min data run. These angular uncertainties translate to radial velocity uncertainties of 2-3 cm/s at radial and angular increments of 2.4 km and 5°. Radial velocity uncertainties *do not* appear to be a fixed percentage of total radial velocity, at least for ARSLOE, where these totals varied between 10 and 50 cm/s. The radial velocity uncertainties *do not* appear to depend strongly on range, remaining the same out to the last range cell recorded with the CODAR (~36 km). They *do* deteriorate in the two 30° sectors nearest to shore (increasing to 3-13 cm/s rms); this is explained by the fewer samples occurring in these sectors, due to increased propagation loss and signal refraction effects.

Two methods were evaluated that provided total velocity vectors and their uncertainties from single-angle CODAR data: model fitting and application of the equation of continuity. The model fitted consisted of a uniform current vector in each of a set of bands parallel to the shore. The model fit does not in fact obey the χ^2 test due to inhomogeneity within the band; it is, however, a convenient way to visualize the results. Statistical uncertainties in the results (which do not include bias due to the inadequate model fit) are typically 4 cm/s, 12°. The spatial resolution (the width of the bands) was chosen so that the accuracy is maintained with range, in spite of decreasing data density; in fact, the results show that we overcompensated for this effect. Several methods were evaluated for the application of the equation of continuity which produced approximately equivalent results. For the closest range cells, uncertainties were about the same as for model fitting (5 cm/s, 12°) but increased rapidly with range to values exceeding 20 cm/s, 30° beyond the 20-km range. This is due to the fact that at the more distant ranges, radial velocities are available only in a limited angular sector because of decreased signal strength. For successful application of the equation of continuity using the methods described, data over the entire angular range is required.

We have verified through analysis of measured sea-echo data that theoretical assumptions made about hardware performance and signal statistics were indeed valid for the ARSLOE experiment. Correlation or coupling between adjacent range cells is ~20 percent, consistent with the slight pulse broadening from the 8-μs nominal value as it passes through the receiver. Correlation between adjacent spectral power frequency points is ~60 percent, as predicted for the Blackman-Harris window applied to the time series; we therefore retained and used every other point for analysis (spaced .00754 Hz apart), and correlation there dropped to ~14 percent, as expected. Correlation between power points at the same frequency for consecutive (but 50 percent overlapped) time-series spectra was effectively zero (i.e., below the 4-percent significance level), so that our assumption (based on theory) of 15 *independent* samples for a 1.2-km-range cell

over the 36 min is valid. The number of degrees of freedom associated with a single power cross-spectral point is slightly higher than the theoretical value for the generalized χ^2 distribution, consistent with a Guassian signal having truncated extrema. The covariance matrix measured from the data agrees with that predicted from theory for N-sampled cross spectra based on Gaussian signals. This verifies the quoted current velocity uncertainties which were calculated using the theoretical expression for the covariance matrix.

a) *Systematic Errors*: Sources of systematic bias in the measured current velocities include the following.

b) Departures of the antenna patterns from the theoretical functions used in the calculations. Such angular biases, described in Section II, are less than the statistical uncertainty in the angle estimates and we conclude, therefore, that they can be ignored.

c) Refraction of radar signals at the coast. This is largest for signals arriving tangential to the coast, which can be displaced as much as 6° out to sea. Statistical uncertainties are also greater in the coastal segments and are in general somewhat larger than the refraction bias.

3) Use of a model which does not adequately fit the data. For example, our analysis will produce biased results if the radial current velocity has the same value at three angles within a range cell, since the model used only allows for two. We note that this is unlikely in normal oceanographic situations. In this event, our results will show gaps in the coverage area and attempts to interpolate across such a gap will produce biased results. Another example could occur in fitting current models to the radial vectors as in Section IV-C. If the χ^2 test is not obeyed, the solution must be regarded as a "forced" average which does not describe all the observed variations of the current pattern.

We note that weather, rain, foam, and whitecaps produce no errors due to propagation and scatter effects in current velocities observed at HF, as can occur at microwave frequencies.

B. Recommendations for Current Measurement with CODAR

In any CODAR system used for current mapping, the fundamental signal-processing operation is the determination of angular patterns associated with the radial velocities defined by the radar spectrum. A great deal of effort has been devoted to this problem and several methods have been employed in the past with varying degrees of success [9], [10], [16]. Actually, the problem (i.e., the estimation of parameters from data containing statistical fluctuations) is extremely common, occurring whenever measured data is interpreted in terms of equations. We have calculated radial current velocities using standard least-squares methods which are generally accepted [18]-[20] to be the optimum way to process noisy data in an objective fashion. These methods produce the fundamental geophysical data product provided by CODAR: radial velocities and their uncertainties over a polar coordinate grid of radar range and bearing. These radial velocity maps must be fully understood by the user, because errors or incorrect assumptions will impact the accuracy and validity of data products from any subsequent analysis. For example, gaps will appear at times in the coverage, where there are no data. Use of subsequent, interpretive routines (e.g., combining data from two sites to get Cartesian vector components, area averaging, space/time filtering, interpolation, extrapolation, trajectory calculations, model fitting, tidal analysis, use of the continuity equation, etc.) is straightforward once the radial map data are properly prepared and understood; on the other hand, blind use of subsequent interpretive routines can produce misleading results that could destroy the credibility of this powerful, ocean remote-sensing tool. All of these subsequent routines, when used, should be applied in a least-squares sense so that a) the applicability of the model/routine to the data can be tested statistically, and b) uncertainties in the output parameters are available, allowing the user to decide how much weight to place in subsequent geophysical interpretations.

Radial velocity maps and their uncertainties should be derived completely automatically and are conveniently produced in real time. For example, the techniques described in this manuscript have been combined in an automatic software package that operates on the sea-echo voltage spectra. These programs a) calculate antenna hardware gain and phase factors from the sea echo, b) separate first from second-order sea echo for each spectrum analyzed, c) apply statistical inference to select the single or dual angle model to best fit the data, d) use least-squares techniques to estimate angles of arrival for each radial velocity component, e) combine the data in an optimal manner to produce maps of radial velocities and their uncertainties. Presently programmed in Fortran and not as yet streamlined in the best operational form, this package nonetheless runs in ~25 percent of the data-acquisition time (36 min) on the same microcomputer that operates the CODAR (PDP 11/23).

The methods developed in this paper were demonstrated for the CODAR loop system, as it operated at ARSLOE. In Appendix E we show how these same methods could be used for extracting currents and their uncertainties from the NOAA 4-element antenna system. However, the CODAR loop system has several advantages over the 4-element system. First, because of lack of pattern symmetries in the 4-element system, less computational efficiency is possible there. Second, significant sidelobes in the 4-element array response pattern can be expected to increase the errors in estimated angles, and hence in the radial velocities. Third, the loop system is considerably more compact physically and will be even more so when the same antenna is used for transmission *and* reception (as is planned in the future); this will also result in an increase in the angular resolution. Finally, methods and software have been demonstrated with the loop system that produce the waveheight directional spectrum simultaneously with the two-dimensional current map [12]. For these reasons, we recommend the replacement of the 4-element by the loop system for all normal CODAR applications and operations.

APPENDIX A
LEAST-SQUARES ANALYSIS TECHNIQUES

Standard data processing texts [18]-[20] show that maximum likelihood provides the optimal method for the extraction of parameters from signals containing statistical fluctuation. Maximum likelihood reduces to the minimization of a weighted quadratic form of the data deviations (known as the

least-squares method) when the data fluctuations appear Gaussian. By the central limit theorem, any data products which are sufficiently sample averaged are effectively Gaussian random variables; this is examined further in Appendix B for the voltage cross-spectral products. Therefore, throughout this analysis, we employ least-squares methods for the extraction of information from data. In this Appendix, we summarize these techniques as we have applied them in our analysis. For a complete treatment, see [20]. In our problem, we have N pieces of data Z_n, $n = 1, 2, \cdots, N$ at N values of an independent parameter x_n and we wish to fit to the data a function of I linear parameters p_i and J nonlinear parameters q_j which is defined by

$$y_n(\bar{p}, \bar{q}) = p_1 f_1(\bar{q}, x_n) + p_2 f_2(\bar{q}, x_n) + \cdots + p_I f_I(\bar{q}, x_n) \tag{A1}$$

where the f_i are known functions. The $(N \times N)$ data covariance matrix C^Z is known.

We form a column matrix of the deviations of the measured data from this functional form

$$\epsilon = \begin{bmatrix} Z_1 - y_1(\bar{p}, \bar{q}) \\ Z_2 - y_2(\bar{p}, \bar{q}) \\ \vdots \\ Z_N - y_N(\bar{p}, \bar{q}) \end{bmatrix}. \tag{A2}$$

The maximum likelihood solution for the parameters p_i, q_j minimizes the quantity

$$I(\bar{p}, \bar{q}) = \epsilon^T G^Z \epsilon \tag{A3}$$

where G^Z is a weight matrix used in the least-squares quadratic form: for the maximum likelihood solution, G^Z is the inverse of the data covariance matrix C^Z; for unity weights as used in (31) and (32), G^Z is the identity matrix.

A. Obtaining the Parameters

1) The Linear Parameters: For any combination of the nonlinear parameters, a closed form solution exists for the optimum linear parameters. The total differential of (A3) with respect to $p_1, p_2, \cdots, p_N$ must vanish; this leads to the relation

$$\bar{p}^* = [A^T G^Z A]^{-1} A^T G^Z \bar{Z} \tag{A4}$$

where the matrices are defined as follows, with the asterisk denoting the optimum value

$$\bar{p}^* = [p_1^*, p_2^*, \cdots p_I^*] \quad A = \begin{bmatrix} f_1(\bar{q}, x_1) \cdots f_I(\bar{q}, x_1) \\ \vdots \quad\quad \vdots \\ f_1(\bar{q}, x_n) \cdots f_I(\bar{q}, x_n) \end{bmatrix}$$

$$\bar{Z} = \begin{bmatrix} Z_1 \\ Z_2 \\ \vdots \\ Z_N \end{bmatrix}.$$

2) The Nonlinear Parameters: After substituting the optimum values for the linear parameters in (A3) (to form $I(\bar{p}^*, \bar{q})$), we performed a grid search over the nonlinear parameters to find the optimum values of $\bar{q}$ that minimize $I(\bar{p}^*, \bar{q})$. There are more efficient methods to locate the minimum involving the linearization of (A1) and/or multidimensional gradient root finders; however, we have not yet found it necessary to implement such methods in our programs.

B. Obtaining the Covariance Matrix

Expanding (A1) as a Taylor series about the optimum gives the approximate expression for the variation in the residual with distance from the optimum

$$\begin{aligned} \Delta y_n = {} & f_1(\bar{q}^*, x_n)\delta p_1 + \cdots + f_I(\bar{q}^*, x_n)\delta p_I \\ & + \left[p_1^* \frac{\partial f_1}{\partial q_1} + \cdots + p_I^* \frac{\partial f_I}{\partial q_1} \right] \delta q_1 \\ & + \cdots + \left[p_1^* \frac{\partial f_1}{\partial p_J} + \cdots + p_I^* \frac{\partial f_I}{\partial q_J} \right] \delta q_J \\ & + \cdots \text{ Higher Order Terms.} \end{aligned} \tag{A5}$$

For the least-squares solution in the vicinity of the optimum values, the parameters minimize the weighted sum of deviations of the measured data including noise from the ideal functional form. In matrix notation

$$(\Delta Z - E\Delta\rho)^T G^Z (\Delta Z - E\Delta\rho) = \min \tag{A6}$$

with

$$\Delta Z = \begin{bmatrix} \Delta Z_1 \\ \Delta Z_2 \\ \vdots \\ \Delta Z_N \end{bmatrix} \quad \Delta\rho = \begin{bmatrix} \delta p_1 \\ \vdots \\ \delta p_I \\ \delta q_1 \\ \vdots \\ \delta q_J \end{bmatrix}$$

where

$$\Delta Z_i = Z_i - y_i(\bar{p}^*, \bar{q}^*)$$

and

$$E = \begin{bmatrix} f_1(\bar{q}^*, x_1) \cdots f_I(\bar{q}^*, x_1) & \left[p_1^* \frac{\partial f_1}{\partial q_1} + \cdots + p_I \frac{\partial f_I}{\partial q_1} \right]_{x_1} & \cdots & \left[p_1^* \frac{\partial f_1}{\partial q_J} + \cdots + p_I \frac{\partial f_I}{\partial q_J} \right]_{x_1} \\ \vdots & \vdots & & \vdots \\ f_1(\bar{q}^*, x_N) \cdots f_I(\bar{q}^*, x_N) & \left[p_1^* \frac{\partial f_1}{\partial q_1} + \cdots + p_I \frac{\partial f_I}{\partial q_1} \right]_{x_N} & \cdots & \left[p_1^* \frac{\partial f_1}{\partial q_J} + \cdots + p_I \frac{\partial f_I}{\partial q_J} \right]_{x_N} \end{bmatrix}$$

The total differential of (A6) with respect to δp_i and δq_j must vanish; this leads to the relation (similar to (A4))

$$\Delta\rho = F\Delta Z \tag{A7}$$

where

$$F = (E^T G^Z E)^{-1} E^T G^Z.$$

Neglecting terms of higher order, the parameter covariance matrix is given by

$$C^\rho = \langle \Delta\rho \Delta\rho^T \rangle = \langle F\Delta Z \Delta Z^T F^T \rangle = F C^Z F^T. \tag{A8}$$

APPENDIX B
THE STATISTICS OF CROSS SPECTRA

Cross spectra occur increasingly frequently in signal processing problems [18]. For example, they are used in the analysis of pitch/roll buoy output to obtain waveheight directional spectra and in data analysis for geophysical prospecting and seismic systems, where cross spectra among separated point sensors are analyzed to determine the source of the signals. Although historically they were computed by initially averaging lagged covariances among the instrument time series and then Fourier transforming, with the advent of digital computers and the FFT, they are now obtained by averaging the conjugate products of the instrument signal complex FFT's. Cross spectra are particularly convenient in the analysis of CODAR multiple-antenna signals. This appendix establishes the properties of cross spectra and their finite sample averages; this is readily accomplished since the HF sea-echo signal voltage (both first and second order) are zero-mean Gaussian random variables [17]. Then, rather than analyzing the unaveraged, complex voltage signals, as has been done in the NOAA CODAR signal-processing software [10], we can preaverage several cross spectra, reducing considerably the noise-like fluctuation in the cross-spectral signal. Such preaveraging of cross spectra is also totally consistent with least-squares methods, for it is easy to show that preaveraging N cross spectra (to reduce the number of terms in the least-squares sum by a factor of N) is equivalent to including all N unaveraged samples in the original sum. The former, however, is much more conservative of machine operations in the numerical least-squares solution. On the other hand, such preaveraging is not possible when fitting models to the actual Gaussian voltages without destroying independent samples and hence information.

Assume that the actual, zero-mean, complex Gaussian nth voltage sample (at each frequency point ω output from the FFT) is defined as

$${}_n\mathring{V}_\alpha = {}_nV_{\alpha r} + i\,{}_nV_{\alpha i} \tag{B1}$$

where ${}_n\mathring{V}_\alpha$ refers to the voltage from the αth sensor. Since the real and imaginary parts ${}_nV_{\alpha r}$ and ${}_nV_{\alpha i}$ are orthogonal, they are both uncorrelated and statistically independent (because they are Gaussian) and have the same variances. Then we can define an N-sample-averaged cross spectrum between the αth and βth sensors as

$${}_n\mathring{C}_{\alpha\beta} \equiv {}_NP_{\alpha\beta} + i\,{}_NQ_{\alpha\beta} = \frac{1}{N}\sum_{n=1}^{N} {}_n\mathring{V}_\alpha\, {}_n\mathring{V}_\beta^* \tag{B2}$$

or

$${}_NP_{\alpha\beta} = \frac{1}{N}\sum_{n=1}^{N} ({}_nV_{\alpha r}\, {}_nV_{\beta r} + {}_nV_{\alpha i}\, {}_nV_{\beta i}) \tag{B3}$$

and

$${}_NQ_{\alpha\beta} = \frac{1}{N}\sum_{n=1} ({}_nV_{\alpha i}\, {}_nV_{\beta r} - {}_nV_{\alpha r}\, {}_nV_{\beta i}). \tag{B4}$$

"P" is often referred to as the cospectrum, while "Q" is termed the quad spectrum. For the CODAR loop system, where $\mathring{V}_\alpha$ represents any of the three antenna signals given by (1)-(3) in this manuscript, it is easy to see that—after mismatch factors have been removed—only cospectra are nonvanishing in the infinite-ensemble limit. (Such is not the case with other instruments; for pitch/roll buoys, for example, where the wave height and slope of sinusoidal components are in time-quadrature with each other, the quad spectrum between these sensor voltages is nonzero while the cospectrum vanishes).

First, we present an outline of the derivation of the probability density of the N-sample-averaged co- and quad spectra defined in (B3) and (B4) and give the result. Define first the infinite-ensemble averaged co- and quad spectra

$$P_{\alpha\beta} \equiv \langle {}_NP_{\alpha\beta} \rangle = \lim_{N\to\infty} {}_NP_{\alpha\beta} \quad Q_{\alpha\beta} \equiv \langle {}_NQ_{\alpha\beta} \rangle = \lim_{N\to\infty} {}_NQ_{\alpha\beta}. \tag{B5}$$

(Note here that we can, of course, have $\alpha = \beta$.) Restricting ourselves to consideration of CODAR signals, we then have $Q_{\alpha\beta} = 0$. Nonetheless, the N-sample-averaged quad spectrum ${}_NQ_{\alpha\beta}$ exists as a zero-mean random variable, and its statistics are examined here also.

a) Express first the quadruply joint Gaussian probability density function for the single Gaussian samples ${}_nV_{\alpha r}$, ${}_nV_{\alpha i}$, ${}_nV_{\beta r}$, ${}_nV_{\beta i}$ with the understanding that correlations between ${}_nV_{\alpha r}$ and ${}_nV_{\alpha i}$, ${}_nV_{\beta r}$ and ${}_nV_{\beta i}$ are both zero, as well as correlations between ${}_nV_{\alpha r}$ and ${}_nV_{\beta i}$, ${}_nV_{\alpha i}$ and ${}_nV_{\beta r}$. Convenient matrix formulations for joint Gaussian probability densities are found in [29] and other texts.

b) Define and determine the characteristic functions of the single-sample co- and quad spectrum. These are the products of

$$\exp\{i\tau({}_nV_{\alpha r}\, {}_nV_{\beta r} + {}_nV_{\alpha i}\, {}_nV_{\beta i})\}$$

and

$$\exp\{i\tau({}_nV_{\alpha i}\, {}_nV_{\beta r} - {}_nV_{\alpha r}\, {}_nV_{\beta i})\}$$

and the joint probability expressed in the previous paragraph, and integrated over the four random variables. Although tedious, these integrations are straightforward because of the mathematical convenience of Gaussian function manipulations,

and may be found in the tables. These characteristic functions are then

$$\Phi_{{}_nP_{\alpha\beta}}(\tau) = \frac{1}{1 - i\tau P_{\alpha\beta} + \frac{\tau^2}{4}(P_{\alpha\alpha}P_{\beta\beta} - P_{\alpha\beta}{}^2)} \tag{B6}$$

$$\Phi_{{}_nQ_{\alpha\beta}}(\tau) = \frac{1}{1 + \frac{\tau^2}{4}(P_{\alpha\alpha}P_{\beta\beta} - P_{\alpha\beta}{}^2)}. \tag{B7}$$

c) The reason for working with the characteristic function is now especially appreciated. The characteristic function of a sum of random variables is merely the product of the individual characteristic functions when they are independent. Because of the scaling factor $1/N$ multiplying each random variable in the N-sample sums of (B3) and (B4), we therefore replace τ in (B6) and (B7) by τ/N and raise the resulting equation to the Nth power.

d) We then Fourier transform the results above back to probability space, to get the density function for ${}_NP_{\alpha\beta}$ and ${}_NQ_{\alpha\beta}$. This is simply done by a contour integration, where residues at the Nth-order poles of the characteristic functions are evaluated. The resulting probability can be expressed as

$$p(x) = \begin{cases} \dfrac{(ab)^N e^{-bx}}{(a+b)^{2N-1}[(N-1)!]^2} \displaystyle\sum_{n=0}^{N-1} (2N-2-n)! \\ \quad \cdot \dbinom{N}{n} x^n (a+b)^n, & \text{for } x \geqslant 0 \\ \dfrac{(ab)^N e^{ax}}{(a+b)^{2N-1}[(N-1)!]^2} \displaystyle\sum_{n=0}^{N-1} (2N-2-n)! \\ \quad \cdot \dbinom{N}{n} (-x)^n (a+b)^n, & \text{for } x < 0 \end{cases} \tag{B8}$$

where $\binom{N}{n}$ are the binomial coefficients, and

$$a \equiv \frac{2N}{\sqrt{P_{\alpha\alpha}P_{\beta\beta}} - P_{\alpha\beta}} \qquad b \equiv \frac{2N}{\sqrt{P_{\alpha\alpha}P_{\beta\beta}} + P_{\alpha\beta}}$$

$$c \equiv \frac{2N}{\sqrt{P_{\alpha\alpha}P_{\beta\beta} - P_{\alpha\beta}{}^2}} = \sqrt{ab}$$

and

$$a + b = \frac{4N\sqrt{P_{\alpha\alpha}P_{\beta\beta}}}{P_{\alpha\alpha}P_{\beta\beta} - P_{\alpha\beta}{}^2}. \tag{B9}$$

Here, x in (B8) represents the N-sample-averaged cospectrum ${}_NP_{\alpha\beta}$, if we use the expressions given for a and b above. On the other hand, x in (B8) represents the quad spectrum ${}_NQ_{\alpha\beta}$ if we let $a = b = c$; but where we have $(a + b)$, replace it with

$$a + b = 2c = \frac{4N}{\sqrt{P_{\alpha\alpha}P_{\beta\beta} - P_{\alpha\beta}{}^2}}.$$

A special case of the above general probability density is the classical χ^2, which is obtained when $\alpha = \beta$ (i.e., $P_{\alpha\alpha} = P_{\alpha\beta} = P_{\beta\beta}$; $a \to \infty$; all other limits are taken appropriately). Thus the χ^2 density describes the sample average of the absolute square of *any* voltage representing sea echo; N independent samples averaged together is a χ^2 random variable with $2N$ degrees of freedom [17], [21]. The χ^2, existing only for the cospectrum ${}_NP_{\alpha\beta}$ in place of x, is nonzero only for positive x; the probability density for the quad spectrum ${}_NQ_{\alpha\beta}$ from (B8) is seen to approach a Dirac delta function centered on $x = {}_NQ_{\alpha\alpha} = 0$, meaning that the quad spectrum is always identically zero (as can be verified from (B4) when $\alpha = \beta$).

Fig. 14 is an example of the probability density of (B8) plotted for $N = 4$. We normalize by defining

$$y \equiv \frac{x}{\sqrt{P_{\alpha\alpha}P_{\beta\beta}}}$$

$$\rho \equiv \frac{P_{\alpha\beta}}{\sqrt{P_{\alpha\alpha}P_{\beta\beta}}}.$$

When $\rho = 1$ we recover the χ^2 density with eight degrees of freedom. The case $N = 4$ is selected for illustration here because it is sufficiently large that the shape of the densities all begin to approach the classic Gaussian shape required as $N \to \infty$ by the Central Limit Theorem; yet $N = 4$ is small enough that some departure from the Gaussian shape is still evident.

We now turn to fourth moments of N-sample-averaged cross spectra; these are required when calculating the covariance matrices used in the text for least-squares and error-propagation purposes. We illustrate the derivation here for the variance of ${}_NP_{\alpha\beta}$, and then merely give the results for all of the remaining covariances, leaving verification to the reader.

First, calculate the average

$$\begin{aligned} \langle {}_NP_{\alpha\beta}{}^2 \rangle &= \frac{1}{N^2} \sum_{n=1}^{N} \sum_{m=1}^{N} \langle ({}_nV_{\alpha r}\, {}_nV_{\beta r} + {}_nV_{\alpha i}\, {}_nV_{\beta i}) \\ &\quad \cdot ({}_mV_{\alpha r}\, {}_mV_{\beta r} + {}_mV_{\alpha i}\, {}_mV_{\beta i}) \rangle \\ &= \frac{1}{N^2} \sum_{n=1}^{N} \sum_{m=1}^{N} [\langle {}_nV_{\alpha r}\, {}_nV_{\beta r}\, {}_mV_{\alpha r}\, {}_mV_{\beta r} \rangle \\ &\quad + \langle {}_nV_{\alpha r}\, {}_nV_{\beta r}\, {}_mV_{\alpha i}\, {}_mV_{\beta i} \rangle \\ &\quad + \langle {}_nV_{\alpha i}\, {}_nV_{\beta i}\, {}_mV_{\alpha r}\, {}_mV_{\beta r} \rangle \\ &\quad + \langle {}_nV_{\alpha i}\, {}_nV_{\beta i}\, {}_mV_{\alpha i}\, {}_mV_{\beta i} \rangle]. \end{aligned}$$

We use the familiar property of averages of Gaussian quadruple products

$$\langle wxyz \rangle = \langle wx \rangle \langle yz \rangle + \langle wy \rangle \langle xz \rangle + \langle wz \rangle \langle xy \rangle$$

to simplify the first term of the above equation, and employ

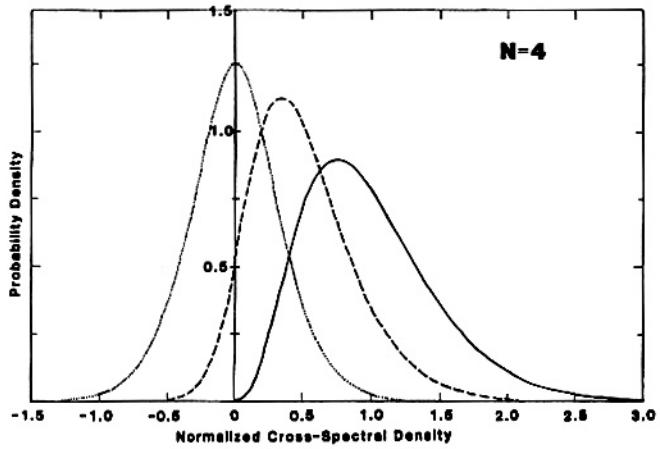

Fig. 14. Probability densities for normalized cross spectra from (B8) with four independent samples averaged. Solid curve has a correlation coefficient ρ between cross-spectral samples of unity; hence it has a normalized mean of unity, a variance of 0.25, and is identically χ^2 with eight degrees of freedom. Dashed line has $\rho = 1/2$, mean = 1/2, variance = 5/32; dotted line has $\rho = 0$, mean = 0, variance = 1/8. Note that for only four cross-spectral samples preaveraged, the probability density functions are already sufficiently close to Gaussian to justify the use of the least-squares representation of maximum likelihood.

the facts that real and imaginary parts are uncorrelated, and different samples are uncorrelated (i.e., when $m \neq n$) to obtain

$$\frac{1}{N^2}\sum_{n=1}^{N}\sum_{m=1}^{N}\langle {}_nV_{\alpha r}\,{}_nV_{\beta r}\,{}_mV_{\alpha r}\,{}_mV_{\beta r}\rangle$$

$$=\frac{1}{4}\left(P_{\alpha\beta}{}^2+\frac{1}{N}P_{\alpha\alpha}P_{\beta\beta}+\frac{1}{N}P_{\alpha\beta}{}^2\right).$$

The last term gives identically the same result. The second term (which gives the same result as the third term) is simplified in the same manner described above to give

$$\frac{1}{N^2}\sum_{n=1}^{N}\sum_{m=1}^{N}\langle {}_nV_{\alpha r}\,{}_nV_{\beta r}\,{}_mV_{\alpha i}\,{}_mV_{\beta i}\rangle=\tfrac{1}{4}P_{\alpha\beta}{}^2.$$

Hence, adding all terms together and subtracting the square of the mean gives

$$\langle {}_NP_{\alpha\beta}{}^2\rangle-\langle {}_NP_{\alpha\beta}\rangle^2=P_{\alpha\beta}{}^2+\frac{1}{2N}P_{\alpha\alpha}P_{\beta\beta}{}^2$$

$$+\frac{1}{2N}P_{\alpha\beta}{}^2-P_{\alpha\beta}{}^2$$

$$\text{Var}\,({}_NP_{\alpha\beta})=\frac{1}{2N}(P_{\alpha\alpha}P_{\beta\beta}+P_{\alpha\beta}{}^2). \tag{B10}$$

We note the familiar property for these cross-spectral variances (and covariances below) of χ^2 sample averages: the fluctuation in the N-sample averages decreases inversely with the number of samples N.

The remaining variances and covariances are similarly established

$$\text{Var}\,({}_NQ_{\alpha\beta})=\frac{1}{2N}(P_{\alpha\alpha}P_{\beta\beta}-P_{\alpha\beta}{}^2) \tag{B11}$$

$$\text{Cov}\,({}_NP_{\alpha\beta}\;{}_NP_{\gamma\delta})=\frac{1}{2N}(P_{\alpha\gamma}P_{\beta\delta}+P_{\alpha\delta}P_{\beta\gamma}) \tag{B12}$$

$$\text{Cov}\,({}_NQ_{\alpha\beta}\;{}_NQ_{\gamma\delta})=\frac{1}{2N}(P_{\alpha\gamma}P_{\beta\delta}-P_{\alpha\delta}P_{\beta\gamma}) \tag{B13}$$

$$\text{Cov}\,({}_NP_{\alpha\beta}\;{}_NQ_{\gamma\delta})=0. \tag{B14}$$

The last three relationships are generalizations of the variances, as we can see by setting $\gamma=\alpha$ and $\delta=\beta$. Also, by using (B12)–which is the same as (17)–we readily establish the covariance matrix for N-sample-averaged ${}_Nb_n(\omega)$ from the definitions (16) to arrive at (18).

APPENDIX C
CALCULATION OF SPECTRAL STATISTICS

In this appendix, we describe a statistical analysis of voltage spectra measured during the ARSLOE experiment. Data used in the analysis were voltage spectra obtained from the three antennas during two 36-min runs–October 24, 05:30 Z (Run 15) and October 25, 16:28 Z (Run 26). The total data set consisted of fifteen spectra (produced by overlapping the time series by 50 percent as described in the text) for each of four 1.2-km range cells lying between 12 km and 16.8 km. The spectra were obtained from a 1024-point FFT, using a Blackman-Harris window. We analyzed the strong signal within ±0.05 Hz of the Bragg frequencies, which is primarily first-order echo but includes some second-order; this defines 54 frequency points with resolution 0.0037 Hz.

Correlation coefficients were calculated as a function of range, frequency separation and time. The correlation coefficient r_k between variables X_i and Y_i, where $i=1,2,\cdots,N$, is defined by

$$r_k=\sum_{i=1}^{N-k}\frac{(x_i-\bar{x})(y_{i+k}-\bar{y})}{(N-k)\sigma_x\sigma_y} \tag{C1}$$

where k is the point separation, $\bar{x}$ and $\bar{y}$ are means, and σ_x and σ_y are standard deviations. The standard error in this quantity is given by

$$\sigma_r=\frac{(1-r_k{}^2)}{\sqrt{N-k-1}}. \tag{C2}$$

To calculate frequency and range correlations, the sum in (C1) was performed over the 15 spectra corresponding to the overlapping times. The mean correlation coefficient over the 54 frequency points was then calculated. For the time correlations, the sum was taken over the 54 frequency points. We give results for the monopole power spectrum in Table VI. Standard errors quoted correspond to zero correlation; it can be seen from (C2) that this defines the maximum value. Equivalent results were obtained for the two loop antennas.

TABLE VI
CORRELATION COEFFICIENTS FOR THE MONOPOLE ANTENNA FREQUENCY CORRELATION

Run	Range (km)	Separation Index 1	2	3	4	5	Maximum Standard Error
15	12.6	.58	.12	.05	.003	.003	.04
	13.8	.62	.19	.11	.06	.01	
	15.0	.61	.12	.04	.05	.03	
	16.2	.60	.11	.02	.02	.01	
26	12.6	.61	.15	.05	.003	.02	
	13.8	.61	.12	.006	.015	.05	
	15.0	.66	.20	.07	.10	.11	
	16.2	.59	.09	.04	.09	.05	
Lies correlation							
15	12.6	-.08	-.06	-.14	-.18	-.04	.14
	13.8	-.02	-.08	-.08	-.08	-.05	
	15.0	-.02	-.08	-.14	-.09	-.10	
	16.2	-.09	-.03	-.18	-.09	-.07	
26	12.6	-.13	-.11	-.05	-.04	-.06	
	13.8	-.05	-.08	-.08	-.15	-.08	
	15.0	.001	-.07	-.05	-.02	-.09	
	16.2	-.03	-.05	-.06	-.08	-.05	
Range Correlation							
15		.22	.08	.02			.04
26		.18	.05	.01			

As a check on the theory, we calculated the number of degrees of freedom in the power spectra measured by the three antennas. As described in the text, this would be two if the voltages were truly Gaussian random variables, but is expected to be greater than two in practice. The number of degrees of freedom in a power spectrum $X(\omega)$ is defined by

$$M = \frac{2\bar{X}(\omega)^2}{\langle [X(\omega) - \bar{X}(\omega)]^2 \rangle}. \tag{C3}$$

This quantity was calculated for the three antennas by performing the ensemble average over the 15 spectra and the 54 frequency points. Results are given in Table VII.

To verify the theoretical expression for the covariance matrix (18) of the text, we first formed cospectra of the voltages and obtained the Fourier angular coefficients as in equation (16). The covariance between two Fourier coefficients is defined by

$$C_{i,j} = \langle [{}_n b_i(\omega) - {}_n\bar{b}_i(\omega)][{}_n b_j(\omega) - {}_n\bar{b}_j(\omega)] \rangle. \tag{C4}$$

This was calculated from the data using the spectra corresponding to different times and ranges to perform the ensemble average. The "theoretical" covariance matrix defined by (18) $C_{i,j}$ was calculated from the voltage cospectra, after they had been averaged over time and range. The two estimates of the covariance matrix were calculated at each frequency. To display the results of the comparison, we calculated the following matrix:

$$R_{i,j} = \frac{(C_{i,j}{}^{\text{th}} - C_{i,j})}{\sqrt{(C_{i,j}{}^{\text{th}2} + C_{i,j}{}^2)/2}} \tag{C5}$$

and formed the mean over the frequency points. The resulting matrix $\bar{R}_{i,j}$ represents the mean weighted deviation between the two estimates and should be small compared with unity. Results are given in Table VIII; only half of the matrix is shown since it is symmetric.

TABLE VII
DEGREES OF FREEDOM PER SPECTRAL POINT

Run	Antenna	Range (km) 12.6	13.8	15.0	16.2
15	1	2.6	2.9	2.8	2.6
	2	2.8	2.8	2.8	2.5
	3	3.0	3.0	2.8	2.6
26	1	2.5	2.6	2.4	3.2
	2	2.5	2.9	2.5	2.4
	3	2.4	2.6	2.7	2.7

TABLE VIII
MEAN DEVIATIONS BETWEEN COVARIANCE MATRIX ESTIMATES

Run	$\bar{R}_{ij}$				
15	.04				
	.06	.02			
	.10	.02	.04		
	.06	.04	.07	.04	
	.05	-.06	-.05	.06	.09
26	-.16				
	.04	.23			
	-.16	-.27	-.32		
	-.10	-.24	-.19	-.26	
	-.07	.17	.00	.01	-.15

APPENDIX D
AUTOMATIC SEPARATION OF THE FIRST-ORDER SPECTRUM

The following procedure was developed for the automatic isolation of the first-order spectrum from which the current velocities are calculated. Frequency boundaries are determined from the nondirectional Fourier coefficient (which is proportional to the monopole power spectrum) for the fifteen range cells independently; these same boundaries are then used for all of the Fourier angular coefficients.

a) The spectrum is first smoothed by taking a running mean of three in frequency.

b) The logarithm of this smoothed spectrum was taken. A new spectrum was formed by calculating the difference between adjacent points in the logarithmic spectrum. We then define the first-order region as lying between the largest positive value of the difference spectrum (defining the left-boundary) and the largest negative value (defining the right-boundary).

c) To be included in the data set for analysis, the spectral power had to exceed 10 times the noise power in the spectrum, which was determined by averaging the spectrum in the region of zero signal; we averaged over frequencies greater than 1 Hz and less than −1 Hz.

d) To be included in the data set, the power had to exceed the maximum spectral power divided by 30, each half of the spectrum being taken separately.

Fig. 7 gives examples of first-order regions defined by these rules. The methods described in this Appendix were developed

to apply to spectra in which the continuum is dominated either by second-order scatter or additive noise, and will work for higher current velocities (i.e., broader first-order spectra) than existed at ARSLOE (as in the Straits of Juan de Fuca [14]).

APPENDIX E
CROSS-SPECTRAL METHODS APPLIED TO MULTIELEMENT MONOPOLE ARRAYS

Working with cross spectra when using least-squares model fitting has the advantage of being able to reduce statistical fluctuation in the data by preaveraging N independent samples (i.e., the cross-spectral data value at a given frequency averaged from N separate time series). This advantage has been recognized and exploited in geophysics, seismic, and oceanic (pitch/roll buoys and wavestaffs) applications, as well as in our own previous analyses of HF radar spectral data. Signals from NOAA's 4-element CODAR monopole antenna array have not been analyzed in this manner in the past. Rather, individual, unaveraged complex voltage samples are processed by closed-form methods to give angle-of-arrival estimates. Besides the several classes of instabilities/singularities in the dual-angle closed-form solutions [10], and their overdetermined (and hence possibly nonunique) nature, calculating angle solutions for each sample and then averaging is numerically more time consuming than preaveraging before angle calculation. Hence, we present in this appendix a formulation and interpretation of 4-element antenna data (applicable also for arbitrary arrays of sensors), so that the methods developed and demonstrated in this paper can be applied directly to that system.

The defining equation we used for the loop system to relate the measured, broad-beam echo pattern $\tilde{\sigma}(\omega, \psi)$ to the narrow-beam pattern $\sigma(\omega, \phi)$ was first presented as [11, (1)] and repeated here as (20). The kernal of the integral relating the two is the antenna beam response pattern

$$\cos^4\left(\frac{\psi-\phi}{2}\right)$$

for the loop system. This antenna system with its reponse pattern has the desirable property of being convolutionally symmetric in ψ and ϕ (and hence completely invariant in shape rotationally). However, any general response pattern can be substituted in its place for arbitrary antenna systems, with only somewhat greater algebraic complexity. The proper beamforming array response pattern to use for an arbitrary receiving point-sensor (monopole) array is [27], [28]

$$g(\psi,\phi)=\left|\frac{1}{K}\sum_{i=1}^{K} a_i e^{i(\bar{k}_\psi-\bar{k}_\phi)\cdot\bar{r}_i}\right|^2 \tag{E1}$$

where for a radar wavenumber $k_0 = 2\pi/\lambda$ (λ being the electrical wavelength), we have

$$\bar{k}_\psi-\bar{k}_\phi=[k_0(\cos\psi-\cos\phi),\ k_0(\sin\psi-\sin\phi)] \tag{E2}$$

with $\bar{r}_i$ being the position vectors from an arbitrary origin to each of the K array elements, and a_i being the weights attached to each of the signals from the K elements.

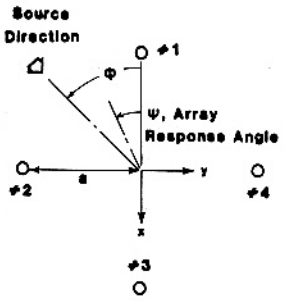

Fig. 15. Sketch of CODAR 4-element receiving antenna array, with spacing "a" from center to elements.

Applied to the NOAA 4-element square array (see Fig. 15), $K = 4$, and $a_i = 1$ (i.e., up to now, no weights have been introduced to modify the response). The pattern can then be expressed as

$$g(\psi,\phi)=\cos^2\left\{\frac{k_0 a}{\sqrt{2}}\left[\sin(\psi-\pi/4)-\sin(\phi-\pi/4)\right]\right\}\cdot\cos^2\left\{\frac{k_0 a}{\sqrt{2}}\left[\cos(\psi-\pi/4)-\cos(\phi-\pi/4)\right]\right\}. \tag{E3}$$

Decomposition of (20)—with $g(\psi, \phi)$ substituted for

$$\cos^4\left(\frac{\psi-\phi}{2}\right)$$

—proceeds more easily if $g(\psi, \phi)$ is expressed as a Fourier series over ψ and ϕ. Unfortunately, because of lack of convolutional symmetry, we require a double series rather than the single series used in (22); furthermore, the series in this case, although it converges fairly rapidly, does not truncate as does (22)

$$g(\psi,\phi)=\sum_m\sum_n g_{mn}tf_m(\psi)tf_n(\phi) \tag{E4}$$

where we give the dominant coefficients g_{mn} for the NOAA system in Table IX (as that system has been operated in the past with $a = \lambda/4$, and hence $k_0 a = \pi/2$). Table X gives the corresponding coefficients for the crossed-loop system.

As we did in the text for the loop system in (23), we similarly define a set of broad-beam coefficients $b_m(\omega)$ here, which are

$$b_m(\omega)=\frac{\pi}{\gamma}\int_{-\gamma}^{\gamma}\sigma(\omega,\phi)\sum_n g_{mn}tf_n(\phi)\,d\phi. \tag{E5}$$

For the first-order sea-echo situation we are treating in this paper, we then arrive at the counterpart here for the two-angle model solution presented in (31)

$$b_m(\omega)=\sum_n g_{mn}[p_1 tf_n(\phi_1)+p_2 tf_n(\phi_2)] \tag{E6}$$

where p_1 and p_2 are identically as defined in (29) of the text. Again, this model is linear in the two unknown amplitudes p_1

TABLE IX
g_{mn} FOR NOAA SQUARE ARRAY

m \ n	-7	-6	-5	-4	-3	-2	-1	0	1	2	3	4	5	6	7
-7	0	0	0	0	.001	0	.001	0	0	0	0	0	0	0	0
-6	0	0	0	0	0	-.002	0	0	0	0	0	0	0	0	0
-5	0	0	.001	0	.011	0	.001	0	0	0	0	0	0	0	0
-4	0	0	0	0	0	0	0	0	0	0	0	0	0	0	0
-3	.001	0	.011	0	.083	0	-.044	0	0	0	0	0	0	0	0
-2	0	-.002	0	0	0	.319	0	0	0	0	0	0	0	0	0
-1	.001	0	.001	0	-.044	0	.346	0	0	0	0	0	0	0	0
0	0	0	0	0	0	0	0	.278	0	0	0	-.078	0	0	0
1	0	0	0	0	0	0	0	0	.346	0	.044	0	.001	0	-.001
2	0	0	0	0	0	0	0	0	0	.236	0	0	0	.007	0
3	0	0	0	0	0	0	0	0	.044	0	.083	0	-.011	0	.001
4	0	0	0	0	0	0	0	-0.028	0	0	0	.028	0	0	0
5	0	0	0	0	0	0	0	0	.001	0	-.011	0	.001	0	0
6	0	0	0	0	0	0	0	0	0	.007	0	0	0	0	0
7	0	0	0	0	0	0	0	0	-.001	0	.001	0	0	0	0

TABLE X
g_{mn} ($=q_n\delta_m{}^n$) FOR CROSSED-LOOP MONOPOLE (RECEIVE)

m \ n			. . .	-2	-1	0	1	2	. . .		
.			.	.	.	.	.	.	.		
.			.	.	.	.	.	.	.		
.	. . .		0	0	0	0	0	0	0	. . .	
-2	. . .		0	.125	0	0	0	0	0	. . .	
-1	. . .		0	0	.500	0	0	0	0	. . .	
0	. . .		0	0	0	.375	0	0	0	. . .	
1	. . .		0	0	0	0	.500	0	0	. . .	
2	. . .		0	0	0	0	0	.125	0	. . .	
.	. . .		0	0	0	0	0	0	0	. . .	
.			.	.	.	.	.	.	.		
.			.	.	.	.	.	.	.		

and p_2, and hence these are readily eliminated before the nonlinear least-squares search for the angle solutions ϕ_1 and ϕ_2.

In terms of the measured, preaveraged cross-spectral data, we have

$$ {}_N\tilde{\sigma}(\omega, \psi) = \frac{1}{K^2} \sum_{i=1}^{K} \sum_{j=1}^{K} {}_N\overset{\circ}{C}_{ij}(\omega) e^{-ik_\psi \cdot (\bar{r}_i - \bar{r}_j)} \qquad \text{(E7)} $$

(in place of (11)), where $\bar{k}_\psi$ is the first vector given in (E2), and ${}_N\overset{\circ}{C}_{ij}$ are the N-sample-averaged cross spectra among the voltage pairs for the four antennas, as defined in (B2). (Again, for the NOAA system $K = 4$ and $\bar{r}_i = -ax, -ay, +ax, +ay$ for $i = 1, 2, 3, 4$, respectively.) Since the above equation is a function of ψ through $\bar{k}_\psi$, the Fourier coefficients $b_m(\omega)$ are evaluated for the data through the use of (14). (Because of the complex way ψ enters (E7), unlike (11) for the crossed loops, no simple separation is possible here like that which led to (16); numerical evaluation of these coefficients from the data is a straightforward procedure, however.) Thus we have N-sample-averaged data coefficients obtained through (E7) which are then least-squares fitted to the single or dual-angle model (E6); the procedure followed is identical to that described in

the text for the loop system. Although the covariance matrix to be used here in estimating statistical uncertainties in the angles is not the same as (18) for that system, it can be obtained in an analogous fashion using the relationships for covariances among N-sampled cross spectra derived in Appendix B and given in (B9)-(B13).

For the loop system, there was no arbitrariness in deciding how many data coefficients $b_n(\omega)$ to use in the least-squares procedure; because (12) contains exactly five terms, there are only five nonzero data coefficients (i.e., $-2 \leqslant n \leqslant +2$). For the NOAA 4-element system, the series describing the measured data, determined here using (E7) in (14), must be truncated at some $|n|$. Table IX suggests that truncating at $|n| = 3$ could result in ~10 percent error/bias because of g_{04} and g_{44} being omitted. Including $|n| = 4$ would leave only ~3 percent truncation error (because of omission of g_{35}, g_{53}, g_{-3-5}, g_{-5-3}). Therefore, data coefficients $b_m(\omega)$ should be calculated and used for $-4 \leqslant m \leqslant +4$. This will result in nearly twice as many terms in the least-squares sums, increasing the computation time; on the other hand, somewhat greater accuracy could be realized with the NOAA 4-element system (for the single-angle case) because of the higher angular resolution of the broad-beam sea-echo pattern $\bar{\sigma}(\omega, \psi)$, represented by the increased number of Fourier coefficients $b_m(\omega)$. We will examine this issue of angular resolution below. Note that the loop system—when used for both transmit *and* receive, as it is to be operated in the future—has a

$$\cos^8\left(\frac{\psi-\phi}{2}\right)$$

pattern which truncates after $-4 \leqslant n \leqslant +4$. Hence it has the same inherent angular resolution as the NOAA 4-element system.

Another difference between the two systems is illustrated in Fig. 16; this shows the antenna response patterns $g(\psi, \phi)$ for signals from three directions: $\phi = 0°$, 22.5°, and 45°. (Because of octant symmetries, these patterns describe responses every 22.5°.) This shows that while the 4-element main beam is narrower than the receive-only beam of the loop system, three undesirable features arise: i) patterns are not rotationally symmetric (i.e., they are different for each signal direction ϕ); ii) response patterns are not symmetric about the input signal direction (e.g., $\phi = 22.5°$); and iii) sidelobe levels are very high in some cases. All of these properties are manifested in the nondiagonal nature and nonsymmetry about the anti-diagonal of g_{mn}, seen in Table IX.

Sidelobes can be reduced somewhat (at the expense of mainlobe broadening) by using nonunity weights a_i in (E1) and (E7). This may be necessary, for in a dual-angle situation (where, for example, a strong signal comes from $\phi_1 = 22.5°$ and a second signal more than 6 dB weaker from another direction), any two-angle fitting procedure could recover a second solution ϕ_2 from the sidelobe maximum of the stronger signal at 235° (see Fig. 16), which is only 5 dB weaker than the main lobe.

We note in passing that a 4-element system of reduced dimensions could theoretically give identically the same pattern and data coefficients $b_n(\omega)$ as the loop system. By forming the difference signal between Elements #1 and #3, for example, we produce in effect a dipole moment (as long as the spacing $2a$ is less than $\lambda/4$). This has an electric field with a cosine angular distribution, analogous to an electrically small loop (which is a magnetic dipole). Therefore, the difference signals between #1 and #3, #2 and #4 produce the same antenna patterns as the two crossed loops; their amplitude factors are different from—and they are in phase quadrature with—the response of each omnidirectional element. Correcting these, one can then accomplish exactly the same effect as for the loop system. Disadvantages to this scheme, however, are: a) the mutual coupling between elements becomes severe when they are this close together; b) shortening the monopole lengths to reduce mutual coupling makes the antennas less efficient; and c) the resulting 4-element system is still larger laterally than the crossed-loop/monopole configuration.

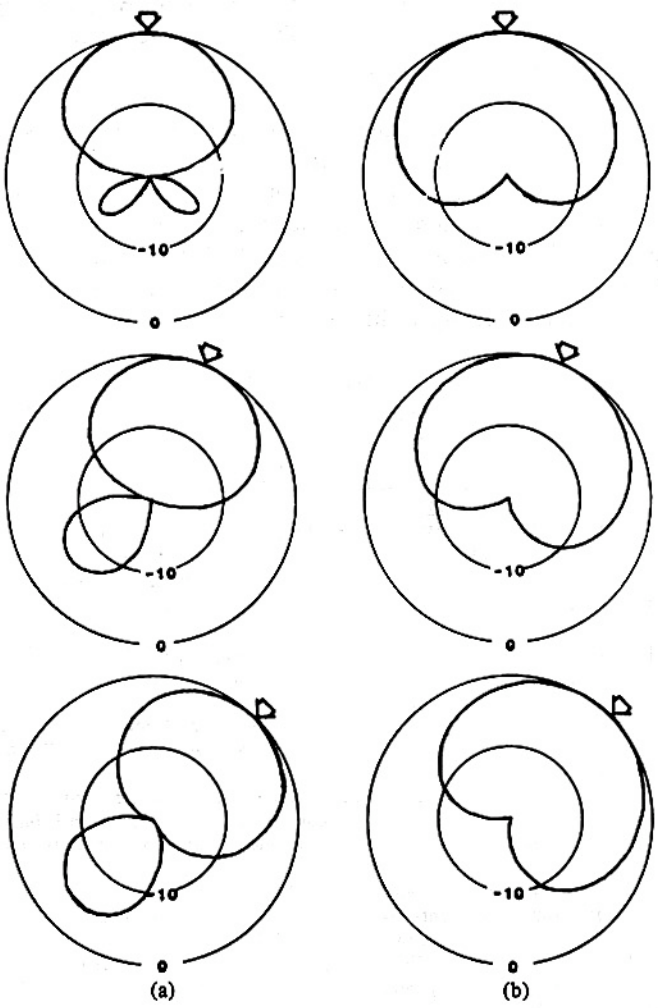

Fig. 16. Calculated response patterns $g(\psi, \phi)$: (a) the CODAR 4-element square array with $a = \lambda/4$ (b) crossed-loop/monopole antenna system (for receive only). Because of the 4-element octant symmetries, these patterns represent source directions, ϕ, every 22.5° around Fig. 15 (the ϕ direction is denoted by the arrow) and power patterns are plotted versus ψ. Circles represent −10-dB levels, with −20 dB at the center.

ACKNOWLEDGMENT

CODAR involvement in the ARSLOE experiment was sponsored by NOAA's Coastal Waves Program, directed by

Dr. L. Baer; this support is greatly appreciated. We gratefully acknowledge partial support for the analysis reported herein from Gulf Oil Exploration and Production Company, whose program is directed by Dr. O. H. Oakley, Jr. and Dr. M. W. Spillane. Design and deployment of the improved crossed-loop/monopole system at ARSLOE was done by A. R. Carr; this antenna is the major hardware advance behind the successes reported herein. Sincere appreciation is extended to M. W. Evans of CODAR Technology, Inc., and D. C. Law of NOAA's Sea State Studies Program for their competent assistance with the hardware and fielding of this experiment.

REFERENCES

[1] D. D. Crombie, "Doppler spectrum of sea echo at 13.56 Mc/s," *Nature*, vol. 175, pp. 681–682, 1955.
[2] D. E. Barrick, "First-order theory and analysis of MF/HF/VHF scatter from the sea," *IEEE Trans. Antennas Propagat.*, vol. AP-20, pp. 2–10, 1972.
[3] D. D. Crombie, "Resonant backscatter from the sea and its application to physical oceanography," in *Oceans '72 Conf. Rec.* IEEE, Publ. no. 72CHO 660-1 OCC, 1972, pp. 173–179.
[4] R. H. Stewart and J. W. Joy, "HF radio measurements of surface currents," *Deep Sea Research*, vol. 21, pp. 1039–1049, 1974.
[5] D. E. Barrick, J. M. Headrick, R. W. Bogle, and D. D. Crombie, "Sea backscatter at HF: interpretation and utilization of the echo," *Proc. IEEE*, vol. 62, pp. 673–680, 1974.
[6] J. W. Maresca, Jr., and C. T. Carlson, "High-frequency skywave radar measurements of Hurricane Anita," *Science*, vol. 209, pp. 1189–1196, 1980.
[7] W. Alpers, J. Schroter, F. Schlude, H. J. Muller, and K. P. Kottermann, "Ocean surface current measurements by an L-band two-frequency microwave scatterometer," *Radio Sci.*, vol. 16, pp. 93–100, 1981.
[8] D. L. Schuler, "Remote sensing of directional gravity wave spectra and surface currents using a microwave dual-frequency radar," *Radio Sci.*, vol. 13, pp. 321–331, 1981.
[9] D. E. Barrick, M. W. Evans, and B. L. Weber, "Ocean surface currents mapped by radar," *Science*, vol. 198, pp. 138–144, 1977.
[10] B. L. Weber and J. A. Leise, "A four-element direction-finding antenna," NOAA Tech. Memo. ERL WPL-99, 1982.
[11] D. E. Barrick and B. J. Lipa, "A compact transportable HF radar system for directional coastal wave field measurements," in *Ocean Wave Climate*, M. D. Earle and A. Malahoff, Eds. New York: Plenum, 1979, pp. 153–201.
[12] B. J. Lipa and D. E. Barrick, "CODAR measurements of ocean surface parameters at ARSLOE—preliminary results," in *Oceans '82 Conf. Rec.* IEEE, Publ. no. 0197-7385/82, 1982, pp. 901–906.
[13] A. S. Frisch and B. L. Weber, "A new technique for measuring tidal currents by using a two-site HF Doppler radar system," *J. Geophys. Res.*, vol. 85, pp. 485–493, 1980.
[14] J. R. Holbrook and A. S. Frisch, "A comparison of near-surface CODAR and VACM measurements in the Strait of Juan de Fuca," *J. Geophys. Res.*, vol. 86, pp. 10 908–10 912, 1981.
[15] M. M. Janopaul, P. Broche, J. C. de Maistre, H. H. Essen, C. Blanchet, G. Grau, and E. Mittelstaedt, "Comparson of measurements of sea currents by HF radar and conventional means," *Int. J. Remote Sensing*, vol. 3, pp. 409–422, 1982.
[16] J. A. Leise, "The analysis and digital signal processing of surface current mapping system," to be published.
[17] D. E. Barrick and J. A. Snider, "The statistics of HF sea-echo Doppler spectra," *IEEE Trans. Antennas Propagat.*, vol. AP-25, pp. 19–28, 1977.
[18] G. M. Jenkins and D. G. Watts, *Spectral Analysis and Its Applications*. San Francisco: Holden-Day, 1968.
[19] P. R. Bevington, *Data Reduction and Error Analysis for the Physical Sciences*. New York: McGraw-Hill, 1969.
[20] S. Brandt, *Statistical and Computational Methods in Data Analysis*. Amsterdam, The Netherlands: North-Holland, 1976.
[21] D. E. Barrick, "Accuracy of parameter extraction from sample-averaged sea-echo Doppler spectra," *IEEE Trans. Antennas Propagat.*, vol. AP-28, pp. 1–11, 1980.
[22] B. J. Lipa and D. E. Barrick, "CODAR measurements of the waveheight directional spectrum in shallow water," in *IGARSS '82 Conf. Rec.*, vol. II. IEEE, 1981, Publ. no. 81CH1656-8, pp. 1107–1113.
[23] J. H. Dunlavy, "Wide-range tunable transmitting antenna," U.S. Patent 3 588 905, June 28, 1971.
[24] A. R. Carr, "Three-element antenna," U.S. Department of Commerce Patent Application 346 314, Feb. 5, 1982.
[25] F. J. Harris, "On the use of windows for harmonic analysis with the Discrete Fourier transform," *Proc. IEEE*, vol. 66, pp. 51–83, 1978.
[26] A. Papoulis, *Probability, Random Variables, and Stochastic Processes*. New York: McGraw-Hill, 1965.
[27] J. Capon, "High-resolution frequency-wavenumber spectrum analysis," *Proc. IEEE*, vol. 57, pp. 1408–1418, 1969.
[28] J. Capon, R. J. Greenfield, and R. J. Kolker, "Multidimensional maximum-likelihood processing of a large seismic array," *Proc. IEEE*, vol. 55, pp. 192–211, 1967.
[29] M. Abramowitz and I. A. Stegun, *Handbook of Mathematical Functions*. Washington, DC: U.S. Government Printing Office, 1964.
[30] A. S. Frisch and J. Leise, "A note on using continuity to extend HF radar surface-current measurements," *J. Geophys. Res.*, vol. 86, pp. 11089–11090, 1981.
[31] H. C. Miller, G. Mason, J. R. Rottier, "Basic environment data summary," CERC-Field Research Facility, Duck, NC, Oct. 1980.

★

Belinda J. Lipa received the B.Sc. and Ph.D. degrees in theoretical physics from the University of Western Australia in 1964 and 1969, respectively, studying the theory of critical point phenomena.

She was a Research Associate at Stanford University from 1974 to 1978, where she was involved in plasma physics investigations, thermodynamics, radar studies of planetary surfaces, and occultation of radio waves through planetary atmospheres. She developed and applied methods for inverting integral equations to obtain geophysical data and their statistical uncertainties. From 1978 to 1980 she was a Senior Research Physicist at SRI International. During the period from 1974 to present, her primary accomplishment has been in the interpretation of HF sea echo to obtain the waveheight directional spectrum and surface currents; she continued this work at Codar Research, a small business she created in 1980. In 1982, she and D. E. Barrick organized a corporation, Ocean Surface Research, to apply radar and other instrumentation to the monitoring and investigation of the ocean surface.

Dr. Lipa is the author or coauthor of 25 open-literature publications.

★

Donald E. Barrick (M'62) received the B.S.E.E. and M.Sc. degrees in 1961 in electrical engineering from the Ohio State University, and the Ph.D. from there in 1965 on the subject of electromagnetic wave scatter from statistically rough surfaces.

Until 1972 he was a Fellow with Battelle's Electromagnetics Division and an Adjunct Professor of Electrical Engineering at the Ohio State University in Columbus, OH. His research involved HF radar, groundwave and ionospheric propagation, signal processing, antennas and scattering, as well as the effects of surface roughness on propagation and scatter. In 1972 he joined NOAA's Wave Propagation Laboratory as Chief of the Sea State Studies Area, where he headed the development of HF radars to the point where they are operational, real-time tools for remotely monitoring ocean waves and currents. He received the U.S. Dept. of Commerce Gold Medal for this work. In 1982, he and B. Lipa organized Ocean Surface Research, Inc., to apply radar and other instrumentation to the monitoring and investigation of the ocean surface.

Dr. Barrick has served the IEEE Antennas and Propagation Society as Associate Editor of the TRANSACTIONS and a member of ADCOM. He was Secretary of URSI Commission F, and is a member of AGU and Sigma Xi. He is coauthor of *Radar Cross Section Handbook*, and some 75 journal articles.